Autism candidate gene *rbm-26* (*RBM26/27*) regulates MALS-1 to protect against mitochondrial dysfunction and axon degeneration during neurodevelopment.

Tamjid A Chowdhury[1], David A Luy[1], Garrett Scapellato[1] Dorian Farache[2,3], Amy SY Lee[2,3], Christopher C Quinn[1*]

[1] Department of Biological Sciences, University of Wisconsin-Milwaukee, Milwaukee, WI, USA.
[2] Department of Cell Biology, Harvard Medical School, Boston, MA, USA.
[3] Department of Cancer Immunology and Virology, Dana-Farber Cancer Institute, Boston, MA, USA.

[*]To whom correspondence should be addressed at: Department Biological Sciences
3209 N. Maryland Avenue
Milwaukee, WI 53211

EMAIL: quinnc@uwm.edu
Phone: (414)229-2602
Fax: (414)229-3926

Abstract

Mitochondrial dysfunction is thought to be a key component of neurodevelopmental disorders such as autism, intellectual disability, and ADHD. However, little is known about the molecular mechanisms that protect against mitochondrial dysfunction during neurodevelopment. Here, we address this question through the investigation of *rbm-26*, the *C. elegans* ortholog of the *RBM27* autism candidate gene, which encodes an RNA-binding protein whose role in neurons is unknown. We report that RBM-26 (RBM26/27) protects against axonal defects by negatively regulating expression of the MALS-1 (MALSU1) mitoribosomal assembly factor. Autism-associated missense variants in RBM-26 cause a sharp decrease in RBM-26 protein expression along with defects in in axon tiling and axon degeneration that occurs during larval development. Using a biochemical screen, we identified the mRNA for the MALS-1 mitoribosomal assembly factor as a binding partner for RBM-26. Loss of RBM-26 function causes a dramatic overexpression of *mals-1* mRNA and MALS-1 protein. Moreover, genetic analysis indicates that this overexpression of MALS-1 is responsible for the mitochondrial and axon degeneration defects in *rbm-26* mutants. These observations reveal a mechanism that regulates expression of a mitoribosomal assembly factor to protect against axon degeneration during neurodevelopment.

Introduction

Emerging evidence suggests an association between mitochondria and neurodevelopmental disorders including autism, intellectual disability, and attention deficit hyperactivity disorder (ADHD). For example, certain mitochondrial DNA lineages confer substantial risk for autism and ADHD [1, 2]. Likewise, heteroplasmic mtDNA mutations are also a risk factor for autism and intellectual disability [3-5]. Consistent with a causative role for mitochondria dysfunction in neurodevelopmental disorders, mice with a hypomorphic missense mutation in the *ND6* mtDNA gene exhibit autism endophenotypes and also produce excess ROS in the brain [6]. In this regard, it is intriguing to note that elevated levels of reactive oxygen species (ROS) have also been observed in autistic human brains [7]. Together, these observations suggest that mitochondrial dysfunction plays a causative role in neurodevelopmental disorders. However, the roles of mitochondrial dysfunction in neurodevelopmental disorders are not well understood.

Some neurodevelopmental syndromes feature neurodegenerative phenotypes that begin during the developmental time period. For example, loss of *EXOSC3* or *EXOSC9* gene function is thought to cause a neurodevelopmental syndrome that includes intellectual disability and axon degeneration during infancy [8-10]. Likewise, loss of the

GAN gene in humans causes the giant axonal neuropathy disease, featuring intellectual disability and axon degeneration in children [11]. Moreover, loss of either the *SPTBN1* or *ADD1* genes are thought to cause a neurodevelopmental syndrome that includes autism and ADHD [12, 13]. In mouse models, variants in these genes cause defects in axon development along with axon degeneration, consistent with a causative role for these genes in the human syndrome [14, 15]. Together, these observations suggest that neurodegeneration may contribute to some neurodevelopmental disorders. However, little is known about the cellular and molecular mechanisms that protect against neurodegeneration in infants and children.

The *RBM27* (*rbm-26*/*Swm*/*Rmn1*) gene encodes an RNA binding protein and is considered an autism candidate gene by the Simmons Foundation Autism Research Initiative (SFARI) [16]. In a cultured human cell line, RBM27 and its paralog RBM26 can function with the PAXT connection, an adaptor complex for the nuclear RNA exosome [17]. Likewise, in *S. pombe* the Rmn1 ortholog of RBM26/27 can also function as part of an adaptor for the nuclear RNA exosome [18]. In *Drosophila,* the Swm ortholog of RBM26/27 has also been implicated in RNA metabolism and the maintenance of adult intestinal stem cells [19]. Despite these findings, the role of RBM27 and its orthologs in neurons have not been investigated. Moreover, the identity of *RBM27* as an autism candidate gene is based on de novo missense mutations that have not been tested for gene-disrupting activity.

Here, we identify a mitochondria-protecting role for the RBM-26 ortholog of RBM26/27 that protects mitochondria and prevents axon degeneration during larval development. We find that loss of RBM-26 function causes a decrease in mitochondrial density in the axon, mitochondrial dysfunction in the cell body, axon degeneration, and transient defects in axon tiling. These phenotypes are induced by an *rbm-26* null allele as well as by alleles that are equivalent to autism-associated de novo missense variants in *RBM27*, suggesting that these are likely gene-disrupting variants in humans. Mechanistically, we identified the *mals-1* mRNA as a binding partner for RBM-26 and found that RBM-26 negatively regulates the expression of the *mals-1* mRNA, which encodes a mitoribosomal assembly factor. Moreover, gain-of-function and loss-of function experiments indicate that MALS-1 is required for both the axon degeneration phenotype and the reduction in axonal mitochondria that are caused by loss of RBM-26. These observations indicate that RBM-26 negatively regulates MALS-1 expression to protect against mitochondrial dysfunction and axon degeneration during development. Based on our findings in *C. elegans*, along with prior work on RBM26/27 [17], we speculate that RBM27 may function with the RNA exosome in humans to protect against neurodevelopmental disorders.

Results

Expression of RBM-26 is disrupted by P80L and L13V missense mutations.

RBM27 has been identified as a candidate autism gene by the Simons Foundation Autism Research Initiative (SFARI) [16]. The potential association of *RBM27* with autism is based on the identification of 5 de novo variants in probands with autism or other neurodevelopmental disorders, but none in unaffected siblings (Fig. 1A) [20-25]. However, the confidence in this association is limited by the fact that the identified variants are all missense variants, rather than likely-gene-disrupting variants. Moreover, a role for *RBM27* in neurodevelopment has not been investigated. To address these issues, we used the *C. elegans rbm-26* ortholog of *RBM27.* We found that 2 of the 5 de novo missense mutation sites in human RBM27 are conserved in *C. elegans rbm-26*. These two conserved missense mutations cause L13V and P79L amino acid changes in human RBM27, which are equivalent to L13V and P80L respectively in *C. elegans* RBM-26 (Fig. 1B). Both of these mutations occur in the PWI-like domains and were identified in genome sequencing studies of children with neurodevelopmental disorders [20, 23].

To determine how the L13V and P80L variants affect RBM-26 protein expression, we used CRISPR to introduce these mutations into the endogenous *rbm-26* gene and also added a 3XFLAG tag to allow for detection by western blot. A sequence encoding 3XFLAG was inserted just upstream of the *rbm-26* stop codon, thereby creating the *rbm-26(cue25)* allele, hereafter referred to as *rbm-26(3XFLAG)*. Next, we used CRISPR to introduce the P80L mutation into the *rbm-26(3XFLAG)* allele, thereby creating the *rbm-26(cue22cue25)* allele, hereafter called *rbm-26(P80L::3XFLAG)*. We also used CRISPR to introduce the L13V mutation into the *rbm-26(3XFLAG)* allele, thereby creating the *rbm-26(cue24cue25)* allele, hereafter called *rbm-26(L13V::3XFLAG)*.

We next used western blotting to detect the RBM-26::3XFLAG, RBM-26 P80L::3XFLAG, and RBM-26 L13V::3XFLAG proteins **(Figure 1C, Figure S1)**. The wild-type RBM-26::3XFLAG protein is predicted to produce proteins with molecular weights around 75 and 82 KD. Consistent with this prediction, we found that the RBM-26::3XFLAG protein was detected as two bands that migrate in between the 72KD and 95KD markers. In addition, we also observed a more intense bands just above the 56KD marker and just above the 95 KD marker as well as two fainter bands in between the 34KD and 56KD markers. The identity of these additional bands are unknown, though it they are likely the result of post-translational processing, or unpredicted splice forms. We found that each of these RBM-26::3XFLAG bands were sharply reduced by the P80L and L13V mutations **(Figure 1C,D)**. To determine if the P80L mutation can reduce expression of RBM-26 in vivo, we used an endogenously tagged *rbm-26::scarlet*

153 gene **(Figure 1E,F)**. Consistent with our western blotting data, we found that the P80L
154 mutation substantially reduces expression of the RBM-26::Scarlet protein in vivo. These
155 observations indicate that the P80L and L13V mutations in *C. elegans rbm-26* sharply
156 reduce RBM-26 expression and imply that the P79L and L13V mutations in human
157 *RBM27* are likely to be gene-disrupting.

158

159 **Mutations in *rbm-26* cause developmental defects in the PLM axon.**

160 To determine if RBM-26 can affect neuronal development, we used the PLM, a neuron
161 that has its cell body in the tail and extends its axon anteriorly along the body wall. The
162 PLM has three presynaptic regions and can also act as a sensor for light touch [26]. In
163 wild type, the PLM axon initially overlaps with the ALM axon during the L1 stage, but
164 this overlap is resolved in later larval stages [26].

165 To determine how loss of RBM-26 function affects the PLM, we used an *rbm-26(null)*
166 mutation, along with *rbm-26(P80L)* and *rbm-26(L13V)* mutations. The *rbm-26(gk910)*
167 null mutation consists of a 408 base pair deletion that removes part of exon 4 and exon
168 5 of *rbm-26* and is lethal. We maintained this *rbm-26(null)* allele over a balancer and
169 found that maternally rescued homozygote progeny are viable until the L3 stage. To
170 study the P80L missense mutation, we used CRISPR to create the *rbm-26(cue23)*
171 allele, hereafter referred to as *rbm-26(P80L)*. We also introduced the L13V missense
172 mutation into the *rbm-26* gene, creating the *rbm-26(cue34)* mutation, hereafter referred
173 to as *rbm-26(L13V)*. In contrast to the *rbm-26(null)* mutation, both the *rbm-26(P80L)* and
174 the *rbm-26(L13V)* mutations are viable.

175 We found that mutations in *rbm-26* cause overlap between the PLM and ALM axons,
176 hereafter referred to as the PLM/ALM overlap phenotype **(Figure 2A-D)**. In *rbm-26(null)*
177 mutants, a greater penetrance of PLM/ALM overlap was observed in the L1, L2 and L3
178 stages relative to wild type. Due to the lethal phenotype of the *rbm-26(null)* mutation, we
179 were unable to analyze PLM axons in in later stages. In the P80L and L13V mutants,
180 we also observed a greater penetrance of PLM/ALM overlap in the L2 and L3 stages
181 relative to wild type. However, we did not observe PLM/ALM overlap at later stages in
182 these missense mutations, suggesting that that these tiling defects resolve at later
183 developmental stages **(Figure 2D)**. Analysis of the PLM axon length to body length ratio
184 suggests that the PLM/ALM overlap phenotype in these three *rbm-26* mutants is caused
185 by overextension of the PLM axon **(Figure S2)**.

186

187 **Mutations in *rbm-26* cause degeneration phenotypes in the PLM axon.**

188 We found that the *rbm-26(null)*, *rbm-26(P80L)*, and the *rbm-26(L13V)* mutations all
189 cause degeneration phenotypes in the PLM axon **(Figures 2E-H and S3; Table S1)**. In
190 the *rbm-26(null)* mutants, we observed a very weak axon beading phenotype in the L2
191 stage that became much stronger in the L3 stage **(Figure 2F)**. The *rbm-26(P80L)*
192 mutation caused an axon beading phenotype that was very weak in the L2 stage,
193 increased in the L3 and L4 stages and became much stronger in the adult stage. We
194 also observed the beading phenotype in *rbm-26(L13V)* mutants, but at a substantially
195 lower penetrance relative to *rbm-26(P80L)*. In addition to beading we observed several
196 other degeneration phenotypes **(Table S1)**, including axon breaks **(Figure 2G,H)**. To
197 determine if loss of *rbm-26* function might cause defects in other neurons, we also
198 observed the PVD neuron and observed signs of degeneration in both its axon and
199 dendrites **(Figure S4)**. These degenerative phenotypes in PLM and PVD are similar to
200 those that have been reported in aging worms [27-29] and are reminiscent of
201 axonopathy that has been reported in human neurodegenerative disorders and
202 described as axonal swellings or spheroids [30-32]. Overall, these observations suggest
203 that RBM-26 protects against axon degeneration. Moreover, these results imply that the
204 P79L and L13V de novo missense mutations in human *RBM27* are likely to disrupt
205 *RBM27* function, thereby supporting a role for this gene in neurodevelopmental
206 disorders.

207

208 **RBM-26 is expressed in multiple tissues and functions within neurons to protect**
209 **against axonal defects.**

210 To visualize the localization of RBM-26, we used CRISPR to insert the coding sequence
211 for a Scarlet::AID (auxin-inducible degron) tag into the 3′ end of the *rbm-26* gene,
212 thereby creating the *rbm-26(*syb2552) allele. We found that this allele expresses RBM-
213 26::Scarlet::AID protein in many tissues including neurons, hypodermis, muscle, and
214 intestine **(Figures 3A-C, S5, and S6)**. Within hypodermis and neurons, we noticed that
215 the RBM-26::Scarlet::AID protein was localized to the nucleus **(Figures 3A-C and S5)**.

216 We next asked where RBM-26 functions to protect against axon degeneration and
217 defects in axon development. For our initial approach to this question, we used the
218 auxin-inducible degron system to selectively degrade the RBM-26::Scarlet::AID protein
219 in in neurons, hypodermis, muscle, and intestine [33]. We found that degradation of
220 RBM-26::Scarlet::AID in neurons caused both PLM/ALM overlap defects **(Figure 3D)**
221 and the PLM beading phenotype **(Fig. 3E)**. However, degradation of RBM-
222 26::Scarlet::AID in hypodermis, muscle, or intestine failed to cause any of these

223 phenotypes **(Figures 3D-E)**. These phenotypes were dependent on auxin and the *rbm-*
224 *26::scarlet::AID* gene **(Figures S7 and S8)**. We also note that both of these phenotypes
225 occurred at a lower penetrance in these degradation experiments relative to
226 experiments with the *rbm-26* mutant alleles, suggesting incomplete degradation of the
227 RBM-26::Scarlet::AID protein.

228 To further test the locus of RBM-26 function, we conducted transgenic rescue
229 experiments. For the transgenic rescue experiments, we used a *Pmec-7::rbm-26*
230 transgene to selectively drive expression of RBM-26 in the touch receptor neurons
231 **(Figures 3F-G)**. We found that this *Pmec-7::rbm-26* transgene could rescue the
232 PLM/ALM axon overlap phenotype in both the *rbm-26(P80L)* mutants and in the *rbm-*
233 *26(L13V)* mutants **(Figure 3F)**. Likewise, the *Pmec-7::rbm-26* transgene could also
234 rescue the beading phenotype in both the *rbm-26(P80L)* mutants and in the *rbm-*
235 *26(L13V)* mutants **(Figure 3G)**.These observations suggest that RBM-26 is broadly
236 expressed and that it functions cell-autonomously within neurons to protect against
237 axon degeneration and defects in axon development.

238

239 **Loss of RBM-26 causes mitochondrial dysfunction.**

240 Mitochondrial dysfunction is thought to be an early causative factor for neuronal
241 degeneration. Therefore, we asked if loss of RBM-26 function affects mitochondria in
242 the PLM. We used the third larval (L3) stage for these experiments, because the *rbm-*
243 *26(null)* mutants die after this stage. We found that mitochondria were localized
244 throughout wild-type PLM axons, with an average density of 9 per 100μm **(Fig. 4A,B,E)**.
245 The *rbm-26(null)* mutation caused a reduction of the mitochondrial density in the PLM
246 axon to about about 6 per 100μm **(Fig. 4C-E)**. Likewise, the *rbm-26(P80L)* and the *rbm-*
247 *26(L13V)* mutations also caused a reduction of the mitochondrial density in the PLM
248 axon **(Fig. 4E)**.To determine the timing of this phenotype, we analyzed *rbm-26(null)*
249 mutants at earlier larval stages and found that the phenotype begins in the L1 stage and
250 persists through the L3 stage, when these mutants die **(Figure 3F)**. We also found that
251 all three *rbm-26* alleles caused a reduction in the number of mitochondria in the
252 proximal axon (50 μM closest to the cell body; see Figure 4G). However, none of the
253 *rbm-26* alleles affected the number of mitochondria in the distal axon (50 μM closest to
254 the axon tip; see Figure 4H). These observations suggest that RBM-26 is needed to
255 maintain a normal density of mitochondria in the proximal PLM axon. We speculate that
256 mitochondria in the proximal PLM axon might be more susceptible to damage because
257 of the higher level of axon transport that occurs in the proximal PLM axon [34].

258 Excess production of reactive oxidation species (ROS) is a key marker for mitochondrial
259 dysfunction [35, 36]. Therefore, we asked if the *rbm-26(null)* mutation causes an
260 increase in ROS production by mitochondria. For this experiment, we used mitoTimer,
261 an oxidation sensor that is tethered to mitochondria and changes irreversibly from green
262 to red as it becomes oxidized [37]. We analyzed the mitoTimer red:green ratio in the
263 PLM cell body because the mitoTImer signal in axons was not sufficient for quantitation.
264 We found that the *rbm-26(null)*, *rbm-26(P80L)*, and *rbm-26(L13V)* mutations all increase
265 the mitoTimer red:green ratio in the PLM cell body relative to wild type **(Figure 5A-E**
266 **and Figure S9)**, suggesting that loss of RBM-26 function causes mitochondria to
267 produce excessive ROS and that RBM-26 is needed to maintain normal mitochondrial
268 function in neurons. Overall, these results suggest that loss of RBM-26 causes
269 dysfunction of mitochondria in the neuronal cell body, which could lead to a decrease in
270 mitochondria density in the axon.

271

272 **RBM-26 binds to the *mals-1* mRNA and negatively regulates its expression.**

273 To understand the molecular mechanisms of RBM-26 function, we conducted a screen
274 to identify RNAs that bind to RBM-26. For this screen, we used ultraviolet light to induce
275 RNA-protein crosslinking in strains expressing RBM-26::3XFLAG and in controls
276 expressing GFP::3XFLAG and Scarlet::3XFLAG (see methods for details). We then
277 used an anti-FLAG antibody to purify the RBM-26::3XFLAG::RNA and
278 Scarlet/GFP::3XFLAG::RNA complexes, followed by RNA-Seq analysis. We identified
279 63 RNAs that were significantly enriched in RBM-26::3XFLAG pulldowns relative to
280 Scarlet/GFP::3XFLAG controls **(Figure 6A and Table S2)**. Among these 63 RNAs we
281 found 26 protein-coding mRNAs, 14 non-coding RNAs, 8 piRNAs, 10 snoRNAs, 1 tRNA
282 and 1rRNA.

283 We focused on the *mals-1* mRNA because it had, by far, the lowest adjusted p-value
284 amongst the RBM-26-binding partners with human orthologs **(Table S2)**. The *mals-1*
285 mRNA encodes an ortholog of the mammalian MALSU1 mitochondrial ribosome
286 assembly factor [38]. Using qPCR, we found that loss of RBM-26 function causes an
287 increase in *mals-1* mRNA expression in *rbm-26(P80L)* and *rbm-26(L13V)* mutants
288 relative to wildtype **(Figure 6B)**. To analyze MALS-1 protein expression, we used
289 CRISPR to add a 3XFLAG tag to MALS-1, thereby creating the *mals-1(cue37)* allele,
290 which expresses the MALS-1::3XFLAG protein. Since the *mals-1* gene is tightly linked
291 to the *rbm-26* gene, we used CRISPR to introduce the P80L mutation into a strain
292 containing the *mals-1(cue37)* mutation, thus creating the *mals-1(cue37) rbm-26(cue42*
293 *[P80L])* double mutant. By performing western blotting to analyze expression of MALS-
294 1::3XFLAG in these strains we found that the *rbm-26(P80L)* mutation substantially

295 enhances expression of the MALS-1::3XFLAG protein relative to wild type **(Figure 6C-**
296 **D)**. We also obtained similar results with the *rbm-26(L13V)* mutation. These
297 observations indicate that RBM-26 negatively regulates the expression of *mals-1* mRNA
298 and MALS-1 protein.

299

300 **Overexpression of MALS-1 phenocopies *rbm-26* loss of function.**

301 Since we found that loss of RBM-26 function causes an increase in MALS-1 expression,
302 we next asked if overexpression of MALS-1 could cause axonal phenotypes. For this
303 experiment, we created the *cueSi36 IV* transgene, hereafter called *Pmec-7::mals-*
304 *1::scarlet* to overexpress MALS-1 in the PLM neuron. Consistent with work on
305 mammalian MALSU1, we found that this overexpressed MALS-1::Scarlet is localized to
306 mitochondria **(Figure 7A-C)**. We found that overexpression of MALS-1 causes an
307 increase in PLM/ALM overlap defects that are significantly greater than those observed
308 in controls **(Figure 7D)**. Overexpression of MALS-1 also caused the axon beading
309 phenotype **(Figure 7E)**. Finally, we found that overexpression of MALS-1 decreases the
310 average density of mitochondria in the PLM axon **(Figure 7F)**. These observations
311 suggest that overexpression of MALS-1 can cause defects that are similar to those
312 caused by loss of RBM-26 function.

313

314 **MALS-1 is required for phenotypes caused by loss of RBM-26 function.**

315 Since loss of *rbm-26* function causes axonal phenotypes and an increase in MALS-1
316 expression, we hypothesized that MALS-1 expression is causative for the axonal
317 phenotypes. To test this hypothesis, we asked if *mals-1* is required for the *rbm-26*
318 mutant phenotypes. For these experiments, we used the *mals-1(syb6330)* allele, a near
319 complete deletion of the *mals-1* coding sequence. We also used the *mals-1(tm12122)*
320 mutation, which is a partial deletion of the *mals-1* coding sequence that is predicted to
321 cause early termination of the MALS-1 protein.

322 To determine if *mals-1* is required for the *rbm-26* mutant phenotypes, we constructed
323 double mutants between alleles of *mals-1* and *rbm-26*. If the *rbm-26* loss of function
324 phenotypes are dependent on *mals-1*, we would expect that the *rbm-26* mutant
325 phenotypes would be suppressed in *rbm-26 mals-1* double mutants relative to *rbm-26*
326 single mutants.

327 Since the *mals-1* and *rbm-26* genes are tightly linked, we used CRISPR to introduce the
328 P80L mutation into a strain containing the *mals-1(syb6330)* mutation, thereby creating
329 the *rbm-26(cue40 [P80L]) mals-1(syb6330)* double mutant. We found that *rbm-*
330 *26(cue40 [P80L]) mals-1(syb6330)* double mutants have significantly lower penetrance
331 of axon beading relative to *rbm-26(P80L)* single mutants **(Figure 8A)**. Likewise, *rbm-*
332 *26(cue40 [P80L]) mals-1(syb6330)* double mutants also have significantly higher
333 mitochondrial density relative to *rbm-26(P80L)* single mutants **(Figure 8B)**. For the
334 PLM/ALM overlap phenotype, we would not expect to see a suppression of the *rbm-*
335 *26(P80L)* phenotype by *mals-1(syb6330)* because *mals-1(syb6330)* single mutants
336 already have this phenotype at a penetrance equal to *rbm-26(P80L)* mutants. However,
337 we did find that *rbm-26(cue40 [P80L]) mals-1(syb6330)* double mutants had a
338 penetrance of axon termination defects that was equal to *mals-1(syb6330)* single
339 mutants **(Figure 8C)**, consistent with the function of *mals-1* and *rbm-26* in a genetic
340 pathway. To further validate these findings, we also repeated these experiments with an
341 independent allele of *mals-1*, *mals-1(tm12122)* and found similar results **(Figure 8A-C)**.
342 We noticed that this *mals-1(tm12122)* allele had slightly higher penetrance of defects
343 relative to the *mals-1(syb6330)* mutant and speculate that this might be the result of an
344 incomplete deletion of the sequence coding for MALS-1 in the *syb12122* allele. Taken
345 together, these observations indicate that the axonal phenotypes of *rbm-26(P80L)* and
346 *rbm-26(L13V)* mutants are dependent on MALS-1 function. Moreover, these
347 observations are consistent with the hypothesis that RBM-26 prevents axon
348 degeneration by negatively regulating expression of MALS-1.

349 We also conducted western blotting as an alternative way to test the interaction
350 between RBM-26, MALS-1, and mitochondria **(Figure 8D-E)**. For this experiment, we
351 used the MRPL-58 mitoribosomal protein as a marker for mitochondria. We found that
352 the *rbm-26(P80L)* mutation causes a significant reduction in amount of MRPL-58
353 protein, consistent with a reduction in the number of mitochondria. We also found that
354 this reduction of MRPL-58 expression was suppressed in *rbm-26(P80L) mals-*
355 *1(syb6330)* double mutants. These observations are consistent with the idea that loss of
356 *rbm-26* causes a reduction in mitochondria that is caused by excessive expression of
357 MALS-1.

358

359 **<u>Discussion</u>**

360 Here, we report that RBM-26 functions in neurons to regulate expression of the MALS-1
361 mitoribosome assembly factor. RBM-26 binds to the *mals-1* mRNA and sharply reduces
362 its expression. Disruptions in this process cause excessive MALS-1 expression, leading
363 to the disruption of mitochondrial function in the developing neuron. These observations

364 provide an example of how post-transcriptional regulation of an mRNA in the nucleus
365 can protect mitochondria in the axon to prevent axon degeneration during neuronal
366 development.

367 We also note that the degenerative and developmental defects caused by loss of *rbm-*
368 *26* function in *C. elegans* larvae are reminiscent of defects in human infants who carry
369 mutations in various components of the RNA exosome [8-10, 39, 40]. Prior work in a
370 human cell line suggests that the RNA exosome functions with the RBM-26/27
371 orthologs of RBM-26 to degrade RNA [17]. Therefore, we speculate that human
372 RBM26/27 could function with the RNA exosome complex to protect against
373 neurodevelopmental defects and axon degeneration in infants.

374

375 **Relationship between axon development defects and axon degeneration**
376 **phenotypes.**

377 We have found that RBM-26 causes defects in both axon development and axon
378 degeneration. This is interesting, because the RBM26/27 orthologs of RBM-26 are
379 thought to function with the RNA exosome [17] and variants in the genes that encode
380 RNA exosome components have been implicated in neurodevelopmental syndromes
381 that also cause defects in both axon development and axon degeneration in children [8-
382 10, 39, 40] (see below for further discussion on the RNA exosome).

383 Axon development defects occur prior to axon degeneration defects in *rbm-26* mutants.
384 Loss of RBM-26 function causes a reduction in mitochondria density that begins during
385 early larval development, coincident with the start of the PLM/ALM overlap phenotype.
386 On the other hand, mitochondrial oxidation is minimal in early larval stages and peaks in
387 later larval stages, coincident with the axon degeneration phenotypes. Overall, these
388 observations suggest that the RBM-26 mutations begin to affect mitochondria in early
389 larval development, giving rise to defects in axon development. In later larval stages,
390 the mitochondrial damage becomes substantially worse, giving rise to axon
391 degeneration.

392 Axon tiling defects are transient in the P80L and L13V missense mutants. The
393 hypomorphic P80L and L13V missense mutations in RBM-26 cause axon tiling defects
394 that start in the early larval stages and are resolved by the 4th larval stage. By contrast,
395 the *rbm-26* null mutation produces the axon tiling defect at a higher penetrance and this
396 phenotype is not resolved. However, the null mutants die prior to the L4 stage, so we
397 are unable to determine if the phenotype would resolve in later stages. We note that in a
398 prior study, we found that neurodevelopmental disease-associated missense mutations

399 in *unc-16* also cause axon tiling defects that are resolved in later stages in *C. elegans*
400 despite causing severe intellectual disability in humans [41]. In this case, *unc-16* null
401 mutations are viable and produce an axon tiling phenotype that persists throughout the
402 life of the worm. On the other hand, a missense mutation in the *egl-19* ortholog of
403 *CACNA1C* produces phenotypes that persist throughout the worm's life [42, 43].
404 Overall, these observations suggest that some, but not all, neurodevelopmental patient-
405 derived mutations can have transient effects in *C. elegans*.

406 **Emerging evidence for the role of the nuclear RNA exosome in the regulation of**
407 **neurodevelopment and neurodegeneration.**

408 The negative regulation of *mals-1* mRNA by RBM-26 may occur through the process of
409 mRNA decay in the nucleus. This idea is supported by our finding that RBM-26 is
410 localized to the nucleus and negatively regulates *mals-1* mRNA. Moreover, prior work in
411 human cells has indicated that RBM26/27 functions with the PAXT complex, an adaptor
412 that delivers polyadenylated RNA to the nuclear RNA exosome for degradation [17]. A
413 similar complex exists in *S. pombe*, where the Rmn1 protein is an ortholog of RBM-26
414 and functions with the MTREC complex, which is orthologous to the PAXT complex
415 [18]. Thus, RBM-26 is part of a highly conserved complex that collaborates with the
416 nuclear RNA exosome to negatively regulate polyadenylated RNA.

417 Although most work on the nuclear RNA exosome complex has focused on non-coding
418 nuclear RNAs, emerging evidence suggests that this complex is also important for the
419 regulation of some mRNAs. For example, in *S. pombe*, the MTREC complex is
420 orthologous to the PAXT complex and is critical for the suppression of meiosis. In this
421 process, the MTREC complex binds to the mRNAs of meiotic genes and delivers them
422 to the nuclear RNA exosome for degradation [44]. In cultured human cells, the *PABPN1*
423 mRNA is degraded by the nuclear RNA exosome, thereby negatively regulating both the
424 *PABPN1 mRNA* and the PABPN protein [45]. In addition, knockdown of RBM26/27 or
425 other members of the PAXT complex in a human cell line can cause upregulation of
426 more than 1000 mRNAs, suggesting that the PAXT complex is able to regulate mRNAs
427 [17]. Consistent with this finding, a group of 360 full length protein-coding mRNAs were
428 identified that are regulated by the nuclear mRNA exosome in a human cell line [46].
429 Together, these observations indicate that the PAXT complex can function with the
430 nuclear RNA exosome to regulate some protein-coding mRNA transcripts.

431 The axon degeneration and axon development phenotypes caused by *rbm-26*
432 mutations are reminiscent of phenotypes caused by mutations in subunits of the human
433 RNA exosome complex. For example, mutations in the *EXOSC3*, *EXOSC8* and
434 *EXOSC9* are thought to cause syndromes that include defects in brain development
435 such as hypoplasia of the cerebellum and the corpus callosum [8-10, 39, 40]. In

436 addition, these syndromes also involve progressive neurodegeneration of spinal
437 neurons that begins in infancy and resembles spinal motor atrophy (SMA). Consistent
438 with these observations, knockdown of EXOSC3, EXOSC8, and EXOSC9 in zebrafish
439 causes brain malformation and axon pathfinding defects [8, 39, 47]. Moreover,
440 mutations in EXOSC3 and EXOSC9 are also associated with intellectual disability in
441 humans [10, 40] and mutations in EXOSC8 causes behavioral defects in zebrafish [39].
442 Together, these observations suggest an important role in for the RNA exosome
443 complex in protecting against neurodegeneration and preventing neurodevelopmental
444 defects.

445

446 **Potential role for MALS-1 overexpression in the disruption of mitoribosome**
447 **biogenesis.**

448 The biogenesis of mitoribosomes is a complex process that involves the assembly of 80
449 proteins and 2 rRNAs into a large subunit (mtLSU) and a small subunit (mtSSU). This
450 process is facilitated by a large number of mitoribosomal assembly factors including
451 RNA processing enzymes, GTPases, RNA helicases, and kinases. MALS-1 is an
452 ortholog of the human MALSU1 mitoribosomal assembly factor that functions as part of
453 the MALSU1:LOR8F8:mtACP anti-association module [48-50]. This module binds to the
454 mtLSU and blocks premature association of mtLSU with mtSSU. Once assembly of
455 mtLSU is complete, MALSU1:LOR8F8:mtACP is released, thereby allowing association
456 of mtLSU with mtSSU. Consistent with these observations, knockdown of MALSU1 in
457 cultured human cells causes mitochondrial dysfunction by disrupting the formation of
458 mitoribosomes [38].

459 Our results suggest that excessive expression of MALS-1 can also disrupt mitochondria.
460 We propose that this disruption of mitochondria occurs because excess MALS-1 can
461 disrupt mitoribosome assembly. This idea is also supported by our finding that loss of
462 *rbm-26* function causes a very high level of MALS-1, the ortholog of MALSU1, a
463 negative regulator of mitoribosome assembly. Moreover, the axon and mitochondrial
464 defects caused by loss of RBM-26 function are dependent on MALS-1 expression. In
465 humans, under normal conditions, MALSU1 binds to mtLSU and prevents it from
466 prematurely assembling with mtSSU [48-50]. After completion of mtLSU assembly,
467 MALSU1 is released, thereby allowing for binding of mtLSU and mtSSU. Extrapolating
468 from the function of MALSU1 in humans, we hypothesize that the high level of MALS-1
469 expression in *rbm-26* mutants may prevent the dissociation of MALS-1 from the mtLSU,
470 thereby interfering with the association between mtLSU and mtSSU.

Although our work suggests that MALS-1 overexpression can cause PLM axon defects, we also observe weaker defects with *mals-1* loss of function mutants. Consistent with this finding, prior work has indicated that knockdown of MALSU1 disrupts mitoribosome assembly and function in human cells [38]. This observation reflects the critical role of MALSU1 in the assembly of the mitoribosomes. Thus, mitochondria can be disrupted by either MALS-1 overexpression or MALS-1 loss of function. We note that the *rbm-26* loss of function defects are substantially stronger than the *mals-1* loss of function defects. Therefore, we propose that the disruption of post transcriptional regulation of mitoribosomal assembly factors may represent a key vulnerability for mitoribosome-associated disease.

Materials and Methods

Strains: The alleles used in this study are listed in **Table S3**. The *rbm-26(gk910)* mutation is lethal and was maintained over the hT2 balancer marked with *bli-4* and *(qIs48)*. Worms used for phenotype analysis were maintained at 20°C on nematode growth medium (NGM) agar plates seeded with OP50 using standard procedures. Worms used for RNA Immunoprecipitation experiments and Western Blotting were cultured on 8P plates seeded with *E. coli* NA22 strain as food source.

Genome editing: Genome editing for *mals-1(syb6330)* and *rbm-26(*syb2552 [*rbm-26::scarlet::AID]*) were performed by SunyBiotech. All other genome editing was performed in our laboratory using a previously described protocol [51, 52]. Guide RNAs and homology directed repair (HDR) templates are listed in Table S4. CRISPR edits were confirmed via PCR and sequencing.

Transgenes: The *cueSi36 IV* transgene encodes *Pmec7::mals-1::scarlet::tbb-2 3'UTR*, *cueSi52 IV* transgene encodes *Pmec-7::rbm-26::scarlet::unc-54 3'UTR*, and the *cueSi35 IV* transgene encodes *Pmec-7:mitoTimer::tbb-2 3'UTR*. A single copy of these transgenes was inserted into the *jsTi1493* landing pad on chromosome IV using the Flp recombinase mediated cassette exchange (RMCE) protocol [53]. The *muIs32* transgene is an integrated multicopy array that encodes *Pmec7::GFP* and was used to visualize the PLM axon. The *jsIs1073* transgene was obtained from Michael Nonet and encodes *Pmec-7::mts:tagRFP* and expresses mitochondria-targeted TagRFP (mitoTagRFP). The *jsIs609* transgene was also obtained from Michael Nonet and encodes *Pmec-7::mts::GFP* and expresses a mitochondria-targeted GFP (mitoGFP) in the PLM neuron.

Analysis of phenotypes: To quantify phenotypes, worms were mounted on a 5% agarose pad, anesthetized with levamisole, and observed with a 40x objective on a

510 Zeiss Axio Imager M2 microscope as previously described [54-57]. For all experiments
511 we observed phenotypes in the L3 stage, since the *rbm-26(null)* mutants don't survive
512 beyond this stage. For many experiments, we also included observations at various
513 other stages from L1 to adult. PLM axons were visualized using the *muIs32 (Pmec-*
514 *7::GFP)* transgene. The PLM/ALM overlap phenotype was scored when the PLM axon
515 tip terminated anteriorly to the ALM cell body. We also captured DIC images of worms,
516 fluorescence images of PLM in the same worms and used ImageJ to quantify the length
517 of the worm and corresponding PLMs. Beading refers to focal enlargement or bubble-
518 like lesions which were at least twice the diameter of the axon in size as shown in
519 Figure S3.
520
521 **Imaging**: Larval stage images displayed in all figures were obtained by mounting on 5%
522 agarose pad, anesthetizing with levamisole, and imaging with a 60x water objective on
523 a Nikon ECLIPSE Ti microscope equipped with the X-Light V2 L-FOV spinning disk
524 system as previously described [58]. NIS-Elements software was used for image
525 acquisition. Image analysis was done with ImageJ or NIS-elements. Identical imaging
526 settings and look-up-tables were used for control and experimental groups. Imaging for
527 mitochondrial counts was done with a 40X oil objective on a Zeiss Axio Imager M2.
528
529 **Analysis of mitoTimer:** All images were captured with identical settings on a
530 spinning disk confocal system (see above). 8-bit images were opened in ImageJ in both
531 red and green channels, the PLM cell body was traced in one channel with the free
532 hand selection tool, and the tracing was restored in the other channel. Raw Integrated
533 Density (RawIntDen) and the area of the region of interest (ROI) was determined in
534 ImageJ. Similarly, RawIntDen and area of a defined background region was obtained.
535 RawIntDen was divided by the area of ROI to obtain total pixel/area. Corrected total
536 pixel/area was obtained by subtracting the background pixel/area from the ROI for both
537 red and green channels.
538
539 **Auxin mediated protein degradation:** Tissue-specific degradation of RBM-
540 26::Scarlet::AID was carried out using the auxin-induced degron (AID) system as
541 previously described [58]. Briefly, Naphthaleneacetic acid (K-NAA) (Phytotechnology
542 Laboratories) was dissolved in double distilled water to obtain 250 mM K-NAA solution
543 and filter-sterilized by passing through 25 mm sterile syringe filter (Pall Corporation).
544 Aliquots from sterile 250 mM K-NAA stock was added to autoclaved and slightly cooled
545 (60°C) NGM to obtain a concentration of 4 mM K-NAA and poured into plates. The next
546 day, 4mM K-NAA plates were seeded with 250 ul *E. coli* OP50 strain. These plates
547 were used within two weeks.
548 To obtain tissue specific degradation, homozygous lines were obtained by crossing
549 *rbm-26(syb2552[rbm-26::Scarlet::AID])* with the following strains: *reSi1 [col-*
550 *10p::TIR1::F2A::mTagBFP2::AID*::NLS::tbb-2 3'UTR]* (for hypodermal degradation),
551 *reSi7 [rgef-1p::TIR1::F2A::mTagBFP2::AID*::NLS::tbb-2 3'UTR]* (for neuronal
552 degradation), *reSi3 [unc-54p::TIR1::F2A::mTagBFP2::AID*::NLS::tbb-2 3'UTR]* (for

553 degradation in muscles), and *reSi12 [ges-1p::TIR1::F2A::mTagBFP2::AID*::NLS::tbb-2*
554 *3'UTR]* (for degradation in intestine).
555 L4 stage *C. elegans* of different genotypes were placed on 4mM K-NAA plates, allowed
556 to grow and lay eggs, L3 stage progenies of the parents initially placed on 4mM K-NAA
557 plates were analyzed for PLM termination defects and PLM beading phenotypes.
558 Knockdown of the RBM-26::Scarlet::AID protein was verified visually. PLMs were
559 visualized with *Pmec-7::GFP* transgene*. rbm-26::Scarlet::AID* without any TIR1 cofactor
560 of AID made up the control group. Knockdown of the RBM-26::Scarlet::AID protein in
561 the PLM was quantified in the same manner as mitoTimer (Figure S10). To elaborate,
562 ImageJ was used to trace PLM in the green channel and the tracing was restored in the
563 red channel. The RawIntDen was recorded for both the channels and subtracted from
564 the background.
565
566 **UV-crosslinking RNA Immunoprecipitation and RNA-Seq**: Worms expressing
567 *wbmIs67* transgene *(eft-3p::3X FLAG::Scarlet::unc-54 3'UTR)* and *wbmIs72* transgene
568 *(pei-1p::3X FLAG::GFP::unc-54 3'UTR)* were used as control group. Control and *rbm-*
569 *26::3X FLAG* worms were grown on NGM plates seeded with *E. coli* OP50 strain until
570 they became gravid, then they were washed in M9 (22mM KH2PO4; 22mM Na2HPO4;
571 85mM NaCl; 1mM MgSO4) and grown for 2 days on 8P plates seeded with *E. coli* strain
572 NA22. 25,000 mixed stages *C. elegans* were washed three times in M9 and placed in
573 an unseeded NGM plate (10 cm) for UV-crosslinking. Plate covers and liquid were
574 removed, and the NGM plates were placed in Spectrolinker X-1000 (Spectronics
575 Corporation) and irradiated with 254 nm UV at energy setting 3000. Worms were then
576 checked under the microscope to ensure that they were immobilized, following which
577 they were washed in M9, and 100,000 worms were collected in 1 ml of RIPA buffer (50
578 mM Tris HCl pH 7.4, 150 mM NaCl, 1% Nonidet NP-40, 0.1% SDS, 0.5% Sodium
579 deoxycholate, Roche cOmplete EDTA-free Protease Inhibitor Cocktail, 25U/ml RNase
580 inhibitor) and homogenized/lysed in BeadBug™3 Microtube homogenizer (40 second
581 homogenization with 1 min rest on ice) at 4°C with 3.2 mm diameter chrome steel beads
582 (8 beads per tube). Lysates were placed in fresh tubes, centrifuged at 16,000 x g for 15
583 minutes at 4°C. The supernatant was saved as lysate and quantified using Pierce BCA
584 Protein Assay kit. 100 ul of Pierce Anti-DYKDDDDK (anti-FLAG) magnetic agarose
585 resin was washed three times in RIPA buffer and added to 1 ml of protein lysate (2
586 mg/ml), incubated overnight at 4°C, and anti-flag agarose bound lysate was separated
587 with the help of a magnet while the supernatant was discarded. The agarose resin was
588 washed once with high salt buffer (50 mM Tris HCl pH 7.4, 1M NaCl, 1 mM EDTA, 1%
589 Nonidet NP-40, 0.1% SDS, 0.5% Sodium deoxycholate, Roche cOmplete EDTA-free
590 Protease Inhibitor Cocktail and RNase Inhibitor) and three times with low salt buffer (20
591 mM Tris HCl pH 7.4, 10mM MgCl2, 0.2% Tween-20, Roche Protease Inhibitor and
592 RNase Inhibitor). To elute RNA, the agarose resin was dissolved in Proteinase K buffer
593 (50 mM Tris-HCl, pH 7.4, 150 mM NaCl, 1 mM MgCl2, 0.05% NP-40, 1% SDS) and
594 incubated with 1.2 mg/ml Proteinase K at 55°C for 30 mins with gentle agitation. RNA
595 was extracted with phenol:chloroform and precipitated with 0.25M Ammonium Acetate,

596 0.12M Lithium Chloride and 85% Ethanol. The pellets were washed with 75% ethanol,
597 dissolved in DEPC-treated water and sent to Azenta US, Inc. for library preparation and
598 RNA sequencing. Raw data obtained from Azenta US, Inc. was analyzed to identify
599 RNA interactors of RBM-26. For RNA-Sequencing pre-processing, adapters were
600 trimmed using Cutadapt [59], and contaminating rRNA reads were removed using
601 bowtie2 [60, 61]. Reads were mapped to the Caenorhabditis elegans transcriptome
602 (Caenorhabditis_elegans.WBcel235) using STAR [62] and differential gene analysis
603 was performed using the DESeq2 package [63] in R Studio. Mapped reads were sorted
604 and indexed using samtools [64].
605
606 **Absolute quantification of *mals-1* mRNA:** 300 N2 wild-type L4 worms and 300 *rbm-*
607 *26* mutants [*rbm-26(cue23)* and *rbm-26(cue34)*] L4 worms were collected in Trizol.
608 Following 5 rounds of freeze thaw on dry ice with 1 min of vortexing during thawing,
609 RNA was extracted as per the manufacturer's protocol.
610 We purchased the following synthetic RNA from Azenta US, Inc:
611 GCACGAAGGAGCACAAAACGAAGCAAUGGAUGGUAUGUCAGUGAGGUGGAAAGA
612 GUUCAGGUGCACG The synthetic RNA was diluted in nuclease free water and the
613 following concentrations were confirmed with Qubit RNA Broad Range Assay Kit
614 (Thermo Fisher Scientific): 10 ng/ul, 1 ng/ul, 0.1 ng/ul, 0.01 ng/ul, 0.001 ng/ul, and
615 0.0001 ng/ul. The diluted RNA standards and 1 ug of total RNA extracted from wildtype
616 and *rbm-26* mutant L4 worms were reverse transcribed with 2µm reverse primer
617 (CGTGCACCTGAACTCTTTCC) and SuperscriptTM First-Strand Synthesis System
618 (Thermo Fisher Scientific) following the manufacturer's protocol. 1µl cDNA was used
619 with 10µl 2x SsoAdvanced Universal SYBR Green Supermix (Biorad) and 5 pmol of the
620 forward *mals-1* primer (TGCACGAAGGAGCACAAAAC) and the reverse *mals-1* primer
621 (CGTGCACCTGAACTCTTTCC). Fluorescence emitted during each cycle was
622 monitored using the CFX96 Touch Real-Timer PCR Detection System (Biorad).
623 Dissociation curve confirmed the presence of a single amplicon. Cycle-to-Threshold (Ct)
624 value of the RNA standards were used to plot a standard curve (R^2 = 0.995) (Figure
625 S11), which was then used to deduce mals-1 mRNA quantity. Data presented here
626 comes from three biological replicates.
627
628 **Western Blotting:** Worms were grown on NGM plates seeded with *E. coli OP50* until
629 gravid, washed in M9, and plated onto 8P plates seeded with *E. coli NA22*. 50,000
630 worms were collected in M9, washed three times and M9 was replaced with RIPA buffer
631 (50,000 worms/1 ml RIPA buffer). Worms were lysed in Bead Bug3™ Microtube
632 homogenizer at 4°C with 3.2 mm chrome steel beads (8 beads/ml RIPA buffer).
633 Following centrifugation at 16000 xg for 15 mins at 4°C, supernatant was saved
634 (snapfrozen) as total protein lysate and snap frozen. Total protein lysates were
635 quantified through BCA assay. 20 – 25 µg of total protein lysate was run on 12% SDS-
636 PAGE, transferred to nitrocellulose membrane (0.2 µm pore). For some experiments, 40
637 µg of total protein lysate was used. The nitrocellulose membrane was incubated with
638 No-stain™ protein labeling reagent for 10 minutes following the manufacturer's

instructions. The membrane was washed 2X in water and 3X in TBST (20 mM Tris, 150 mM NaCl, 0.1 % Tween-20). Then, the membrane was blocked in 5% non-fat milk in TBST, probed with primary antibody, washed 3X in TBST, probed with secondary antibody, washed in 3X in TBST, developed with Super Signal West PICO Plus (Thermo Fisher Scientific) and imaged with iBright CL1500 (Thermo Fisher Scientific). The iBright CL 1500 on-instrument analysis software and No-Stain Labeled Membrane setting was used for normalization. iBright analysis software was used for band intensity quantification, which was reevaluated with ImageJ. Antibodies used in this study are listed in supplemental table S4.

Acknowledgements

We thank Michael Nonet, Shohei Mitani, and the Caenorhabditis Genetics Center (funded by NIH P40 OD010440) for strains. We also thank Claire de la Cova and Mark McBride for sharing equipment, Claire de la Cova for assistance with imaging experiments and Scott Aoki for help with the UV-RIPseq experiments. This work was funded by the National Institute of Mental Health grant R01MH119157 (to CCQ), the National Institute of Neurological Disorders and Stroke grant R03NS101524 (to CCQ), Discovery and Innovation Grant (101X432) from the University of Wisconsin - Milwaukee (to TAC) and National Institutes of Health grant 1R35GM142527 (to ASYL). This article does not represent the official views of the National Institutes of Health and the authors bear sole responsibility for its content.

Figure 1: Expression of RBM-26 is disrupted by P80L and L13V missense mutations. (A) Putative protein domains in human RBM27, and *C. elegans* RBM-26 proteins predicted by NCBI's CD-Search. CCCH-type Zn Finger domains (Green Rectangles) and RNA Recognition Motifs (Gold Pentagons) were predicted with high confidence by NCBI's CD-Search and SMART database. PWI superfamily (Blue Hexagon) was predicted by NCBI's CD-Search with high confidence. Red arrows indicate de novo missense variants identified in patients with autism or other neurodevelopmental disorders. (B) Clustal Omega alignment of the N-terminus of the human RBM27 and *C. elegans* RBM-26 proteins. Two de novo RBM27 variants, L13V and P79L (red arrows), were found in regions conserved in *C. elegans* RBM-26. (C) Representative western blot of three biological replicates showing expression of RBM-26::3XFLAG, RBM-26 P80L::3XFLAG and RBM-26 L13V::3XFLAG proteins. 20 µg of total protein lysate was loaded per well and specific proteins were detected with an anti-

679 FLAG antibody and enhanced chemiluminescence. Protein loading was quantified by
680 No-Stain™ Protein Labeling Reagent. (D) Densitometric quantification of protein bands.
681 Statistical significance was analyzed by one-way ANOVA with a Tukey post hoc test,
682 **p<0.01. (E) Example of endogenously tagged RBM-26 in wild type at the L3 stage. (F)
683 Example of endogenously tagged RBM-26 in *rbm-26(P80L)* mutant at the L3 stage.
684 RBM-26 was endogenously tagged with Scarlet using CRISPR to generate the *rbm-*
685 *26(syb2552[rbm-26::Scarlet::AID]) allele.* CRISPR was used to insert the P80L mutation
686 into *rbm-26 (syb2552)* to create the *rbm-26(cue48[rbm-26(P80L)] syb2552[rbm-*
687 *26::Scarlet::AID])* allele.
688
689
690
691 **Figure 2: Mutations in *rbm-26* cause axon degeneration and defects in axon tiling.**
692 (A) Example of a normal PLM axon, where the PLM axon does not overlap with the ALM
693 axon (B) Diagram of the touch receptor neurons. (C) Example of an axon tiling defect
694 (PLM/ALM overlap phenotype), where the PLM axon overlaps with the ALM axon. Axon
695 beading can also be seen (asterisk). (D) Quantification of axon tiling defects in various
696 stages. (E) Example of axon beading phenotype (asterisks) in an *rbm-26(null)* mutant.
697 (F) Quantification of beading phenotype at various stages. (G) Example of the axonal
698 break phenotype in the PLM of a two-day old adult *rbm-26 (P80L)* mutant. (H)
699 Quantification of the axonal break phenotype at various stages. Asterisks indicate
700 statistically significant difference relative to wild type, Z-test for proportions (***
701 p<0.0001, ** p<0.01 and * p<0.05), and error bars represent the standard error of the
702 proportion. Scale bars are 10 µm. Axons are visualized with the *muIs32 (Pmec-7::gfp)*
703 transgene. Stages are labeled with L1(first larval stage), L2(second larval stage,
704 L3(third larval stage), L4(fourth larval stage), 1-Day Adult and 2-Day Adult. Alleles: *rbm-*
705 *26(null)* is *rbm-26(gk910)*; *rbm-26(P80L)* is *rbm-26(cue23)*; *rbm-26(L13V)* is *rbm-*
706 *26(cue34)*.
707
708 **Figure 3: RBM-26 is expressed in the PLM and functions within neurons to**
709 **protect against axon degeneration and prevent defects in axon tiling.**
710 (A) PLM is identified by GFP expression driven by the *muIs32* transgene that encodes
711 *Pmec-7::gfp*. (B) Expression of endogenously tagged RBM-26. The endogenously
712 tagged allele of RBM-26 is *rbm-26 [syb2552(rbm-26::Scarlet::AID)].* A and B are merged
713 in C. (D & E) Neuron-specific degradation of RBM-26::Scarlet::AID causes the
714 PLM/ALM overlap phenotype and axon beading. However, degradation in hypodermis,
715 muscle and intestine do not cause these phenotypes. Control strain is *rbm-*

716 *26::Scarlet::AID*. (F & G) The PLM/ALM overlap and the beading phenotypes caused by
717 mutations in *rbm-26* are rescued by the expression of the *Pmec-7::rbm-26::Scarlet*
718 transgene, which expresses RBM-26 in PLM and other touch receptor neurons.
719 Asterisks indicate statistically significant difference, Z-test for proportions (* $p<0.05$,
720 ***$p<0.001$), and error bars represent the standard error of the proportion. "n" is 150 for
721 in D and E and 200 in F and G. Touch receptor neurons were visualized in D – G with
722 the *muIs32* transgene.
723
724
725
726 **Figure 4: Loss of RBM-26 function causes a reduction in the density of**
727 **mitochondria in the PLM axon.**
728 (A-E) RBM-26 loss of function reduces the number of mitochondria in the PLM axon. (A-
729 B) Example of mitochondria (arrowheads) in an L3 wild-type PLM. (C-D) Example of
730 mitochondria in *rbm-26(null)* L3 PLM. PLM axons are visualized with the *muIs32*
731 transgene that encodes *Pmec-7::gfp* and mitochondria are visualized with *jsIs1073*
732 transgene that encodes *Pmec-7::mito:RFP*. B & D show mitochondria only. Images are
733 from the middle of the PLM axon. Scale bars are 10 μm. (E) Quantification of the
734 density of mitochondria (number of mitochondria per 100 μm of PLM axon) in axons at
735 the L3 stage ($n \geq 25$). Statistical significance was analyzed by one-way ANOVA with a
736 Tukey post hoc test, **$p<0.01$. (F) Quantification of the density of mitochondria (number
737 of mitochondria per 100 μm) in L1, L2 and L3 PLM axons. 20 PLMs were analyzed for
738 L1 and L2, and 25 PLMs were analyzed for L3. Statistical significance was analyzed by
739 two-tailed Student's t-test. The reduction in the number of mitochondria in PLM axons in
740 the *rbm-26* mutants was limited to the proximal PLM axon (50μm closest to the cell
741 body) (G) and was not observed in the distal PLM axon (50 μm closest to the axon tip)
742 (H). 20 PLMs were observed for each genotype in G and H. Statistical significance was
743 analyzed by one-way ANOVA with a Tukey *post hoc* test, ** $p < 0.01$, ns = not
744 significant. Error bars in E – H are the standard error of mean. Alleles: *rbm-26(null)* is
745 *rbm-26(gk910)*; *rbm-26(P80L)* is *rbm-26(cue23)*; *rbm-26(L13V)* is *rbm-26(cue34)*.
746
747 **Figure 5: Loss of RBM-26 causes mitochondria dysfunction in PLM.** RBM-26 loss of
748 function causes excess oxidative activity in mitochondria. To detect oxidative activity in
749 mitochondria, we used mitoTimer, which is a green fluorescent protein when newly
750 synthesized but shifts to red fluorescence when oxidized. (A-A'') Example of mitoTimer
751 expression in an L3 wild-type PLM cell body. (B-B'') Example of mitoTimer expression in an
752 L3 *rbm-26(null)* mutant PLM cell body. Scale bars are 4 μm. (C–E) Quantification of the ratio

753 of red to green mitoTimer expression in *wt* and *rbm-26* mutant PLM cell bodies in different
754 larval stages. Statistical significance was analyzed by one-way ANOVA with a Tukey post
755 hoc test (*p<0.05, **p<0.01 and ns = not significant). "n" is 30 for C and E, and 21 for D.
756 Error bars represent the standard error of mean. The mitoTimer transgene is *cueSi35 IV*
757 *(Pmec-7::mitoTimer::tbb-2 3'UTR)*. Alleles: *rbm-26(null)* is *rbm-26(gk910)*; *rbm-*
758 *26(P80L)* is *rbm-26(cue23)*; *rbm-26(L13V)* is *rbm-26(cue34)*.
759
760 **Figure 6: RBM-26 binds to the *mals-1* mRNA and negatively regulates its**
761 **expression.**
762
763 (A) RNA interactors of RBM-26 as identified by UV-RIPseq (see methods for details).
764 Data generated from three biological replicates. (B) Loss of RBM-26 function increases
765 expression of the *mals-1* mRNA. Absolute levels of *mals-1* mRNA quantified using real-
766 time RT-PCR (see methods for details). Graph represents averages of three biological
767 replicates. Error bars are standard deviations. Asterisks indicate statistically significant
768 difference relative to wild type, two-tailed Student's t-test (***p<0.0001). (C) Loss of
769 RBM-26 function causes an increase in MALS-1 protein expression. Wildtype worms
770 are *mals-1(cue37)* that expresses MALS-1::3X FLAG. CRISPR was used to insert P80L
771 and L13V mutations into the *mals-1(cue37)* chromosome generating *rbm-26(cue40)*
772 *mals-1(cue37)* and *rbm-26(cue49) mals-1(cue37),* respectively. 20 µg of total protein
773 lysate from a mixed stage population was loaded per well in the top panel and specific
774 proteins were detected with an anti-FLAG antibody and enhanced chemiluminescence.
775 Loading was assessed with No-Stain™ protein labeling reagent. 40 µg of total protein
776 lysate was loaded for wild-type and *rbm-26(cue40) mals-1(cue37)* mutants in bottom
777 panels. (D) Densitometric quantification of MALS-1 protein levels in western blots. Data
778 are expressed as mean ± S.E.M. from three independent experiments. Asterisks
779 indicate statistically significant difference relative to wild type, two-tailed Student's t-test
780 (**p<0.01,*p<0.05)
781
782
783 **Figure 7: Overexpression of MALS-1 reduces mitochondria in the PLM axon and**
784 **causes axon degeneration and defects in axon tiling.**
785
786 (A-C) Overexpressed MALS-1::Scarlet protein colocalizes with mitochondria. (A)
787 Mitochondria visualized with the *jsIs609* transgene, which expresses a mitochondria-
788 targeted GFP (mitoGFP) in the PLM neuron. (B) MALS-1::Scarlet expressed by the
789 *cueSi36 IV* transgene. (C) Merged image showing colocalization of MALS-1::Scarlet

790 with mitoGFP. (D-F) Overexpression of MALS-1::Scarlet causes defects similar to those
791 caused by loss of RBM-26 function. (D) Axon tiling defects caused by MALS-1::Scarlet
792 overexpression. (E) PLM axon beading phenotype caused by MALS-1::Scarlet
793 overexpression. (F) Decrease in mitochondria density (number of mitochondria per 100
794 µm) in the PLM axon caused by MALS-1::Scarlet overexpression. Asterisks in panels D
795 and E indicate statistically significant difference relative to wild type, Z-test for
796 proportions (**p<0.01, ***p<0.0001). For panels D and E, error bars represent the
797 standard error of the proportion. Statistical significance in panel F was analyzed by
798 Student's t-test, ***p<0.001 and error bars represent the standard error of mean.
799
800
801 **Figure 8: Loss of MALS-1 function suppresses the mitochondrial and axon**
802 **degeneration phenotypes that are caused by loss of RBM-26 function.**
803
804 (A) Loss of *mals-1* function suppresses the PLM axon beading phenotype caused by
805 the *rbm-26* mutations. (B) Loss of *mals-1* function suppresses the reduction of
806 mitochondria caused by the *rbm-26* mutations. (C) Loss of *mals-1* function causes PLM
807 axon termination defect but fails to enhance PLM axon termination defects caused by
808 the *rbm-26* mutations. The *rbm-26(cue40 [P80L]) mals-1(syb6330)* double mutant was
809 created by introducing the P80L mutation into the *mals-1(syb6330)* mutant
810 chromosome. The *rbm-26(cue41 [P80L]) mals-1(tm12122)* double mutant was created
811 by introducing the P80L mutation into the *mals-1(tm12122)* mutant chromosome. The
812 *rbm-26 (cue47 [L13V]) mals-1(syb6330)* double mutant was created by introducing the
813 L13V mutation into the *mals-1(syb6330)* mutant chromosome. Asterisks in A and C
814 indicate statistically significant difference, Z-test for proportions (*p<0.05, **p<0.01, ***
815 p<0.0001). For panels A and C, error bars represent the standard error of the proportion
816 (n = 200). For panel B, error bars represent the standard error of the mean (n=25), and
817 statistical significance was analyzed by one-way ANOVA with a Tukey post hoc test
818 (*p<0.05 and **p<0.01). (D) Loss of RBM-26 protein expression causes a decrease in
819 mitoribosome expression, which was assayed with the MitoRibo-Tag system consisting
820 of the MRPL-58 mitoribosomal protein tagged at its C-terminus with 3XFLAG (MRPL-
821 58::3XFLAG). This MRPL-58::3XFLAG protein was expressed by the *mrpl-58(cue38)*
822 allele, which was created by CRISPR. *mrpl-58(cue38) rbm-26(cue39)* double mutant
823 was created by introducing the P80L mutation into *mrpl-58(cue38)* by CRISPR. CRISPR
824 was also used to insert a 3X FLAG tag at the C-terminus of MRPL-58 in *mals-*
825 *1(syb6330)* mutant to create *mrpl-58(cue50) mals-1(syb6330)*. Finally, *rbm-26 (P80L)*
826 mutation was inserted into *mrpl-58(cue50) mals-1(syb6330)* to create *rbm-26(cue51*

827 *[P80L]) mrpl-58(cue50) mals-1(syb6330).* 25 µg of total protein lysate from mixed stage
828 population were loaded per lane and specific proteins were detected with an anti-FLAG
829 antibody and enhanced chemiluminescence. Protein loading was analyzed by No-
830 stain™ protein labeling reagent. (E) Densitometric quantification of MRPL-58 protein
831 levels in western blots. Data are expressed as mean ± S.E.M. from three biological
832 replicates. Asterisks indicate statistically significant difference relative to wild type,
833 Student's t-test (*p<0.05).
834
835
836 **Literature Cited**
837
838

839 1. Chalkia, D., et al., *Association Between Mitochondrial DNA Haplogroup Variation and*
840 *Autism Spectrum Disorders.* JAMA Psychiatry, 2017. **74**(11): p. 1161-1168.
841 2. Chang, X., et al., *Mitochondrial DNA haplogroups and risk of attention deficit and*
842 *hyperactivity disorder in European Americans.* Transl Psychiatry, 2020. **10**(1): p. 370.
843 3. Valiente-Palleja, A., et al., *Genetic and clinical evidence of mitochondrial dysfunction in*
844 *autism spectrum disorder and intellectual disability.* Hum Mol Genet, 2018. **27**(5): p.
845 891-900.
846 4. Wang, Y., et al., *Association of mitochondrial DNA content, heteroplasmies and inter-*
847 *generational transmission with autism.* Nat Commun, 2022. **13**(1): p. 3790.
848 5. Wang, Y., M. Picard, and Z. Gu, *Genetic Evidence for Elevated Pathogenicity of*
849 *Mitochondrial DNA Heteroplasmy in Autism Spectrum Disorder.* PLoS Genet, 2016.
850 **12**(10): p. e1006391.
851 6. Yardeni, T., et al., *An mtDNA mutant mouse demonstrates that mitochondrial deficiency*
852 *can result in autism endophenotypes.* Proc Natl Acad Sci U S A, 2021. **118**(6).
853 7. Liu, X., et al., *Oxidative Stress in Autism Spectrum Disorder-Current Progress of*
854 *Mechanisms and Biomarkers.* Front Psychiatry, 2022. **13**: p. 813304.
855 8. Burns, D.T., et al., *Variants in EXOSC9 Disrupt the RNA Exosome and Result in Cerebellar*
856 *Atrophy with Spinal Motor Neuronopathy.* Am J Hum Genet, 2018. **102**(5): p. 858-873.
857 9. Wan, J., et al., *Mutations in the RNA exosome component gene EXOSC3 cause*
858 *pontocerebellar hypoplasia and spinal motor neuron degeneration.* Nat Genet, 2012.
859 **44**(6): p. 704-8.
860 10. Zanni, G., et al., *Exome sequencing in a family with intellectual disability, early onset*
861 *spasticity, and cerebellar atrophy detects a novel mutation in EXOSC3.* Neurogenetics,
862 2013. **14**(3-4): p. 247-50.
863 11. Shirakaki, S., R.R. Roshmi, and T. Yokota, *Genetic Approaches for the Treatment of Giant*
864 *Axonal Neuropathy.* J Pers Med, 2022. **13**(1).
865 12. Cousin, M.A., et al., *Pathogenic SPTBN1 variants cause an autosomal dominant*
866 *neurodevelopmental syndrome.* Nat Genet, 2021. **53**(7): p. 1006-1021.

13. Qi, C., et al., *Variants in ADD1 cause intellectual disability, corpus callosum dysgenesis, and ventriculomegaly in humans.* Genet Med, 2022. **24**(2): p. 319-331.
14. Leite, S.C., et al., *The Actin-Binding Protein alpha-Adducin Is Required for Maintaining Axon Diameter.* Cell Rep, 2016. **15**(3): p. 490-498.
15. Lorenzo, D.N., et al., *betaII-spectrin promotes mouse brain connectivity through stabilizing axonal plasma membranes and enabling axonal organelle transport.* Proc Natl Acad Sci U S A, 2019. **116**(31): p. 15686-15695.
16. Abrahams, B.S., et al., *SFARI Gene 2.0: a community-driven knowledgebase for the autism spectrum disorders (ASDs).* Mol Autism, 2013. **4**(1): p. 36.
17. Silla, T., et al., *The human ZC3H3 and RBM26/27 proteins are critical for PAXT-mediated nuclear RNA decay.* Nucleic Acids Res, 2020. **48**(5): p. 2518-2530.
18. Zhou, Y., et al., *The fission yeast MTREC complex targets CUTs and unspliced pre-mRNAs to the nuclear exosome.* Nat Commun, 2015. **6**: p. 7050.
19. Ariyapala, I.S., et al., *The RNA-binding protein Swm is critical for Drosophila melanogaster intestinal progenitor cell maintenance.* Genetics, 2022. **222**(2).
20. Deciphering Developmental Disorders, S., *Prevalence and architecture of de novo mutations in developmental disorders.* Nature, 2017. **542**(7642): p. 433-438.
21. Homsy, J., et al., *De novo mutations in congenital heart disease with neurodevelopmental and other congenital anomalies.* Science, 2015. **350**(6265): p. 1262-6.
22. Iossifov, I., et al., *The contribution of de novo coding mutations to autism spectrum disorder.* Nature, 2014. **515**(7526): p. 216-21.
23. Krumm, N., et al., *Excess of rare, inherited truncating mutations in autism.* Nat Genet, 2015. **47**(6): p. 582-8.EXOSC
24. Turner, T.N., et al., *denovo-db: a compendium of human de novo variants.* Nucleic Acids Res, 2017. **45**(D1): p. D804-D811.
25. Zhou, X., et al., *Integrating de novo and inherited variants in 42,607 autism cases identifies mutations in new moderate-risk genes.* Nat Genet, 2022. **54**(9): p. 1305-1319.
26. Gallegos, M.E. and C.I. Bargmann, *Mechanosensory neurite termination and tiling depend on SAX-2 and the SAX-1 kinase.* Neuron, 2004. **44**(2): p. 239-49.
27. Pan, C.L., et al., *Genetic analysis of age-dependent defects of the Caenorhabditis elegans touch receptor neurons.* Proc Natl Acad Sci U S A, 2011. **108**(22): p. 9274-9.
28. Tank, E.M., K.E. Rodgers, and C. Kenyon, *Spontaneous age-related neurite branching in Caenorhabditis elegans.* J Neurosci, 2011. **31**(25): p. 9279-88.
29. Toth, M.L., et al., *Neurite sprouting and synapse deterioration in the aging Caenorhabditis elegans nervous system.* J Neurosci, 2012. **32**(26): p. 8778-90.
30. Burke, R.E. and K. O'Malley, *Axon degeneration in Parkinson's disease.* Exp Neurol, 2013. **246**: p. 72-83.
31. Yong, Y., et al., *Axonal spheroids in neurodegeneration.* Mol Cell Neurosci, 2021. **117**: p. 103679.

907 32. Yuan, P., et al., *PLD3 affects axonal spheroids and network defects in Alzheimer's disease.*
908 Nature, 2022. **612**(7939): p. 328-337.
909 33. Martinez, M.A.Q. and D.Q. Matus, *Auxin-mediated Protein Degradation in*
910 *Caenorhabditis elegans.* Bio Protoc, 2020. **10**(8).
911 34. Drozd, C.J. and C.C. Quinn, *UNC-116 and UNC-16 function with the NEKL-3 kinase to*
912 *promote axon targeting.* Development, 2023. **150**(18).
913 35. Murphy, M.P., *How mitochondria produce reactive oxygen species.* Biochem J, 2009.
914 **417**(1): p. 1-13.
915 36. Schon, E.A. and S. Przedborski, *Mitochondria: the next (neurode)generation.* Neuron,
916 2011. **70**(6): p. 1033-53.
917 37. Laker, R.C., et al., *A novel MitoTimer reporter gene for mitochondrial content, structure,*
918 *stress, and damage in vivo.* J Biol Chem, 2014. **289**(17): p. 12005-12015.
919 38. Rorbach, J., P.A. Gammage, and M. Minczuk, *C7orf30 is necessary for biogenesis of the*
920 *large subunit of the mitochondrial ribosome.* Nucleic Acids Res, 2012. **40**(9): p. 4097-109.
921 39. Boczonadi, V., et al., *EXOSC8 mutations alter mRNA metabolism and cause*
922 *hypomyelination with spinal muscular atrophy and cerebellar hypoplasia.* Nat Commun,
923 2014. **5**: p. 4287.
924 40. Di Donato, N., et al., *Mutations in EXOSC2 are associated with a novel syndrome*
925 *characterised by retinitis pigmentosa, progressive hearing loss, premature ageing, short*
926 *stature, mild intellectual disability and distinctive gestalt.* J Med Genet, 2016. **53**(6): p.
927 419-25.
928 41. Drozd, C.J., T.A. Chowdhury, and C.C. Quinn, *UNC-16 interacts with LRK-1 and WDFY-3 to*
929 *regulate the termination of axon growth.* Genetics, 2024.
930 42. Buddell, T., et al., *An autism-causing calcium channel variant functions with selective*
931 *autophagy to alter axon targeting and behavior.* PLoS Genet, 2019. **15**(12): p. e1008488.
932 43. Buddell, T. and C.C. Quinn, *An autism-associated calcium channel variant causes defects*
933 *in neuronal polarity in the ALM neuron of C. elegans.* MicroPubl Biol, 2021. **2021**.
934 44. Harigaya, Y., et al., *Selective elimination of messenger RNA prevents an incidence of*
935 *untimely meiosis.* Nature, 2006. **442**(7098): p. 45-50.
936 45. Bergeron, D., et al., *Regulated Intron Retention and Nuclear Pre-mRNA Decay Contribute*
937 *to PABPN1 Autoregulation.* Mol Cell Biol, 2015. **35**(14): p. 2503-17.
938 46. Wu, M., et al., *The RNA exosome shapes the expression of key protein-coding genes.*
939 Nucleic Acids Res, 2020. **48**(15): p. 8509-8528.
940 47. Giunta, M., et al., *Altered RNA metabolism due to a homozygous RBM7 mutation in a*
941 *patient with spinal motor neuropathy.* Hum Mol Genet, 2016. **25**(14): p. 2985-2996.
942 48. Brown, A., et al., *Structures of the human mitochondrial ribosome in native states of*
943 *assembly.* Nat Struct Mol Biol, 2017. **24**(10): p. 866-869.
944 49. Cheng, J., O. Berninghausen, and R. Beckmann, *A distinct assembly pathway of the*
945 *human 39S late pre-mitoribosome.* Nat Commun, 2021. **12**(1): p. 4544.

50. Rebelo-Guiomar, P., et al., *A late-stage assembly checkpoint of the human mitochondrial ribosome large subunit.* Nat Commun, 2022. **13**(1): p. 929.
51. Buddell, T. and C. Quinn, *A null allele in the wdfy-3 selective autophagy gene of C. elegans.* MicroPubl Biol, 2022. **2022**.
52. Ghanta, K.S., T. Ishidate, and C.C. Mello, *Microinjection for precision genome editing in Caenorhabditis elegans.* STAR Protoc, 2021. **2**(3): p. 100748.
53. Nonet, M.L., *Efficient Transgenesis in Caenorhabditis elegans Using Flp Recombinase-Mediated Cassette Exchange.* Genetics, 2020. **215**(4): p. 903-921.
54. Xu, Y. and C.C. Quinn, *MIG-10 functions with ABI-1 to mediate the UNC-6 and SLT-1 axon guidance signaling pathways.* PLoS Genet, 2012. **8**(11): p. e1003054.
55. Xu, Y. and C.C. Quinn, *Transition between synaptic branch formation and synaptogenesis is regulated by the lin-4 microRNA.* Dev Biol, 2016. **420**(1): p. 60-66.
56. Xu, Y., et al., *Axon response to guidance cues is stimulated by acetylcholine in Caenorhabditis elegans.* Genetics, 2011. **189**(3): p. 899-906.
57. Xu, Y., et al., *SYD-1C, UNC-40 (DCC) and SAX-3 (Robo) function interdependently to promote axon guidance by regulating the MIG-2 GTPase.* PLoS Genet, 2015. **11**(4): p. e1005185.
58. Fischer, N.C., et al., *The ANC-1 (Nesprin-1/2) organelle-anchoring protein functions through mitochondria to polarize axon growth in response to SLT-1.* PLoS Genet, 2022. **18**(11): p. e1010521.
59. Kechin, A., et al., *cutPrimers: A New Tool for Accurate Cutting of Primers from Reads of Targeted Next Generation Sequencing.* J Comput Biol, 2017. **24**(11): p. 1138-1143.
60. Langmead, B. and S.L. Salzberg, *Fast gapped-read alignment with Bowtie 2.* Nat Methods, 2012. **9**(4): p. 357-9.
61. Langmead, B., et al., *Scaling read aligners to hundreds of threads on general-purpose processors.* Bioinformatics, 2019. **35**(3): p. 421-432.
62. Dobin, A., et al., *STAR: ultrafast universal RNA-seq aligner.* Bioinformatics, 2013. **29**(1): p. 15-21.
63. Love, M.I., W. Huber, and S. Anders, *Moderated estimation of fold change and dispersion for RNA-seq data with DESeq2.* Genome Biol, 2014. **15**(12): p. 550.
64. Li, H., et al., *The Sequence Alignment/Map format and SAMtools.* Bioinformatics, 2009. **25**(16): p. 2078-9.

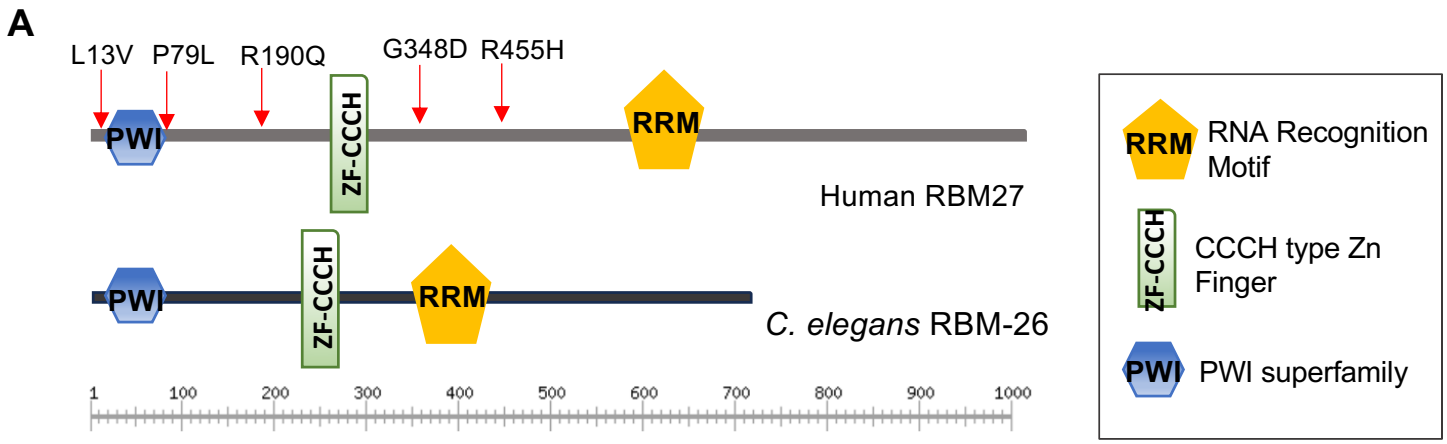

B

L13V - Human

```
MLIEDVDALKSWLAKLLEPICDADPSALANYVVALVKK-DKPEKELKAFCADQLDVFLQK 59
MHIDNEDALFDWLSDELSPITDADPNALAKYVLALVKKPDKGHDELKAFTNEQLNVFLTD 60
* *:: *** .**:. *.** ****.***:**:***** ** ..*****  :**:*** .
```

Human RBM27
C. elegans RBM-26

L13V - *rbm-26 (cue23)*

P79L - Human

```
ETSGFVDKLFESLYTKNYLPLLEPVKPEPKPLVQEKEEIKEEVF--QEPAE-EERDGRKK 116
HTAPFVDKVFEALTSKSYMPASTAPTSASATA----PDLKKEKAPAEKPSKPTAPPGVQK 116
.*: ****:**:* :*.*:*     .           ::*:*    ::*::     * :*
```

Human RBM27
C. elegans RBM-26

P80L - *rbm-26 (cue23)*

C

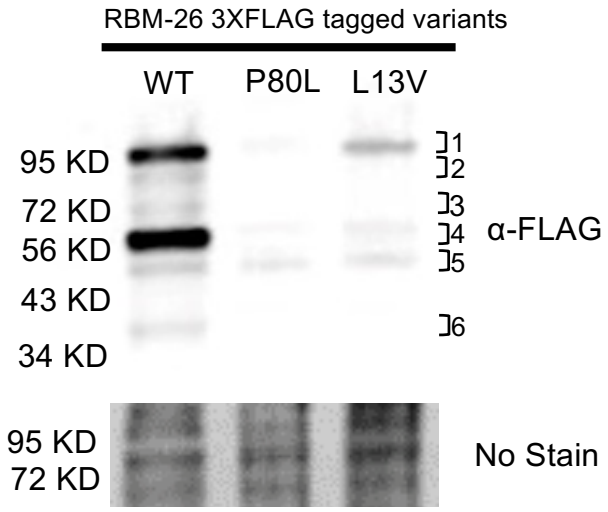

D

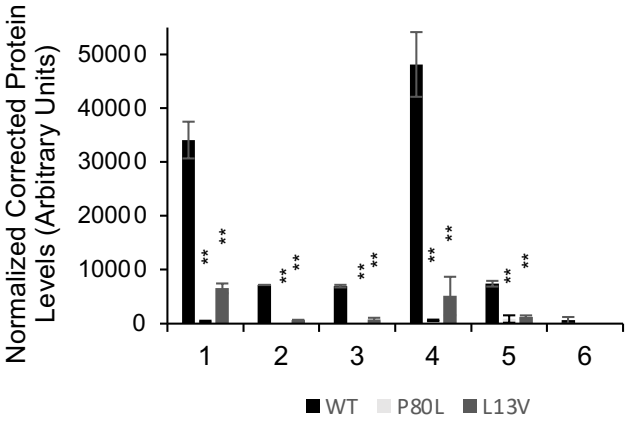

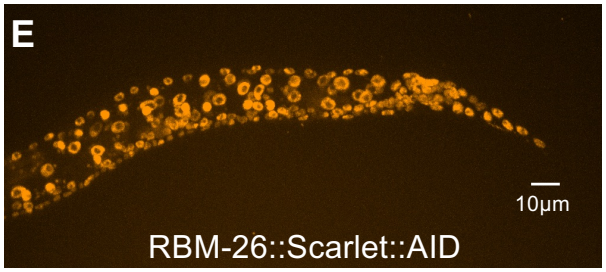

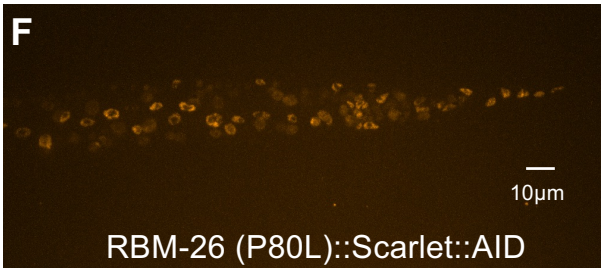

Figure 1

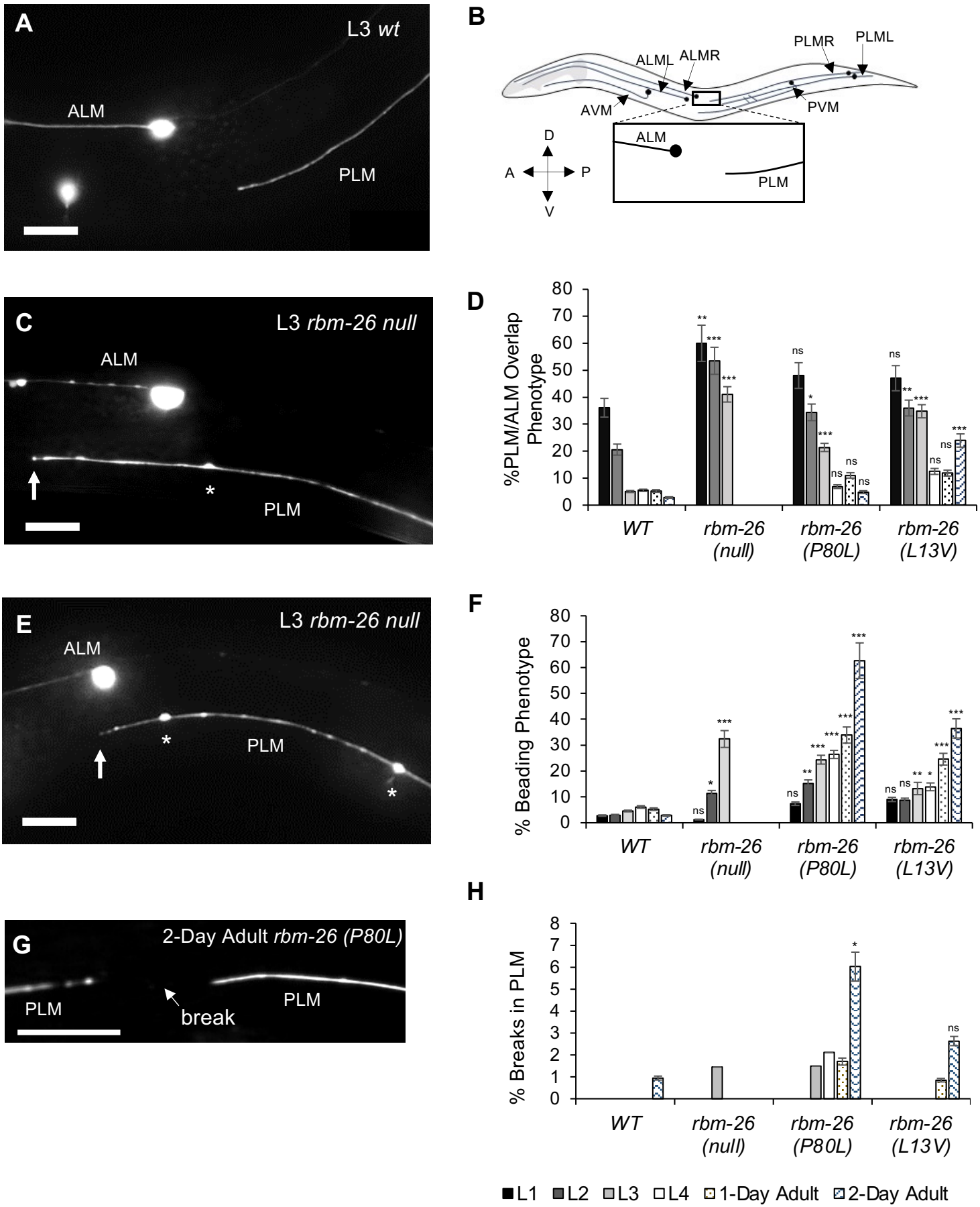
A
L3 wt
ALM
PLM
B
ALML
ALMR
PLMR
PLML
AVM
PVM
D
A
P
V
ALM
PLM
C
L3 rbm-26 null
ALM
PLM
D
%PLM/ALM Overlap Phenotype
WT
rbm-26 (null)
rbm-26 (P80L)
rbm-26 (L13V)
E
L3 rbm-26 null
ALM
PLM
F
% Beading Phenotype
WT
rbm-26 (null)
rbm-26 (P80L)
rbm-26 (L13V)
G
2-Day Adult rbm-26 (P80L)
PLM
break
PLM
H
% Breaks in PLM
WT
rbm-26 (null)
rbm-26 (P80L)
rbm-26 (L13V)
L1
L2
L3
L4
1-Day Adult
2-Day Adult

Figure 2

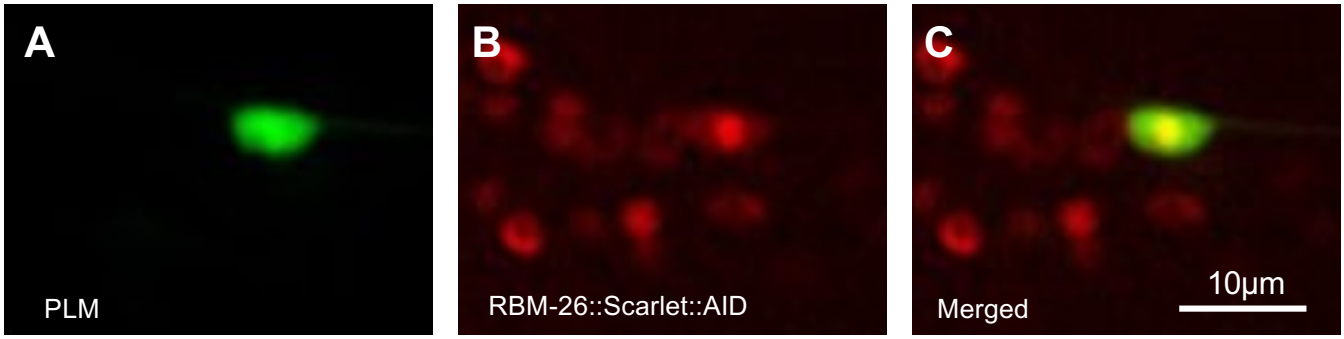
A
PLM
B
RBM-26::Scarlet::AID
C
Merged
10µm

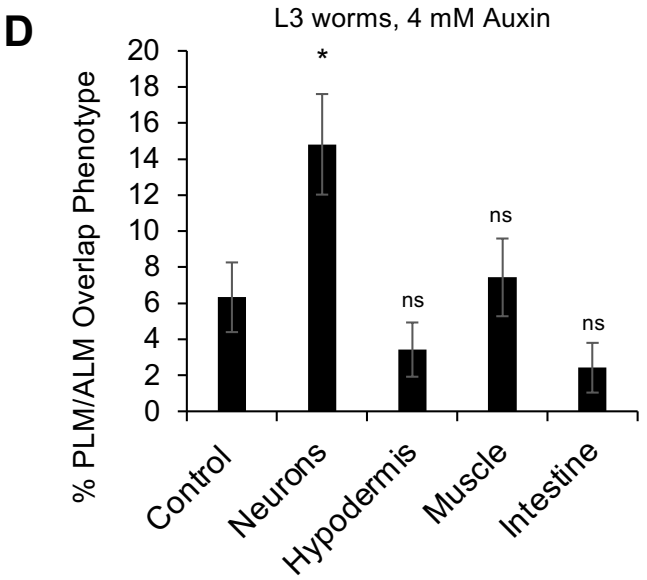
D
L3 worms, 4 mM Auxin
% PLM/ALM Overlap Phenotype
20
18
16
14
12
10
8
6
4
2
0
*
ns
ns
ns
Control
Neurons
Hypodermis
Muscle
Intestine

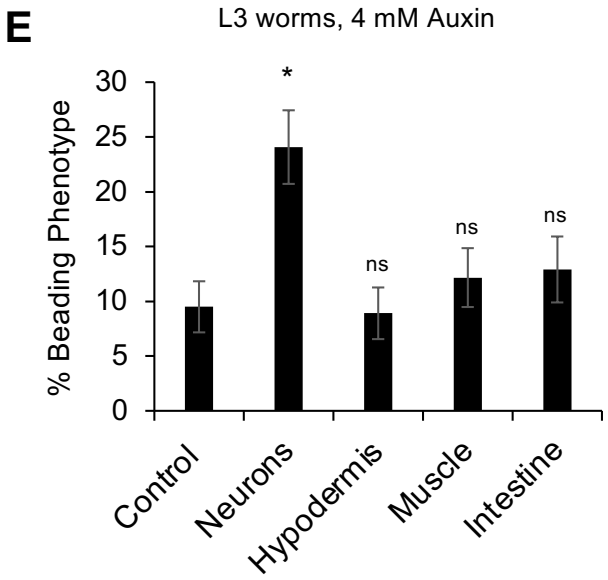
E
L3 worms, 4 mM Auxin
% Beading Phenotype
30
25
20
15
10
5
0
*
ns
ns
ns
Control
Neurons
Hypodermis
Muscle
Intestine

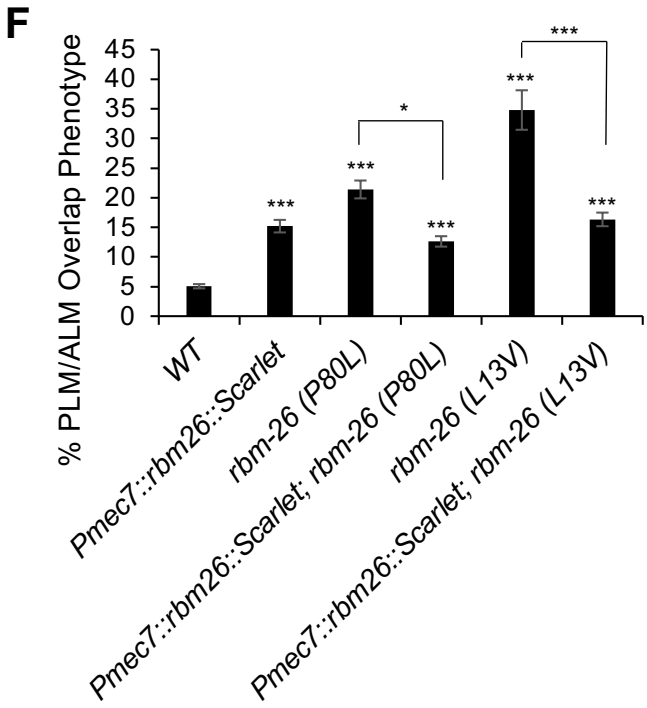
F
% PLM/ALM Overlap Phenotype
45
40
35
30
25
20
15
10
5
0
***
***
*
***
***
***
***
WT
Pmec7::rbm26::Scarlet
rbm-26 (P80L)
Pmec7::rbm26::Scarlet; rbm-26 (P80L)
rbm-26 (L13V)
Pmec7::rbm26::Scarlet; rbm-26 (L13V)

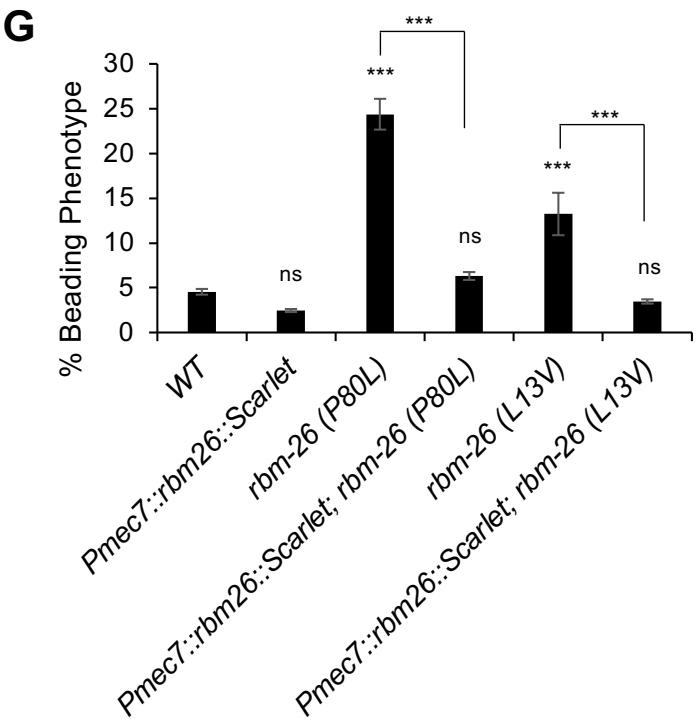
G
% Beading Phenotype
30
25
20
15
10
5
0
ns
***
***
ns
***
***
ns
WT
Pmec7::rbm26::Scarlet
rbm-26 (P80L)
Pmec7::rbm26::Scarlet; rbm-26 (P80L)
rbm-26 (L13V)
Pmec7::rbm26::Scarlet; rbm-26 (L13V)

Figure 3

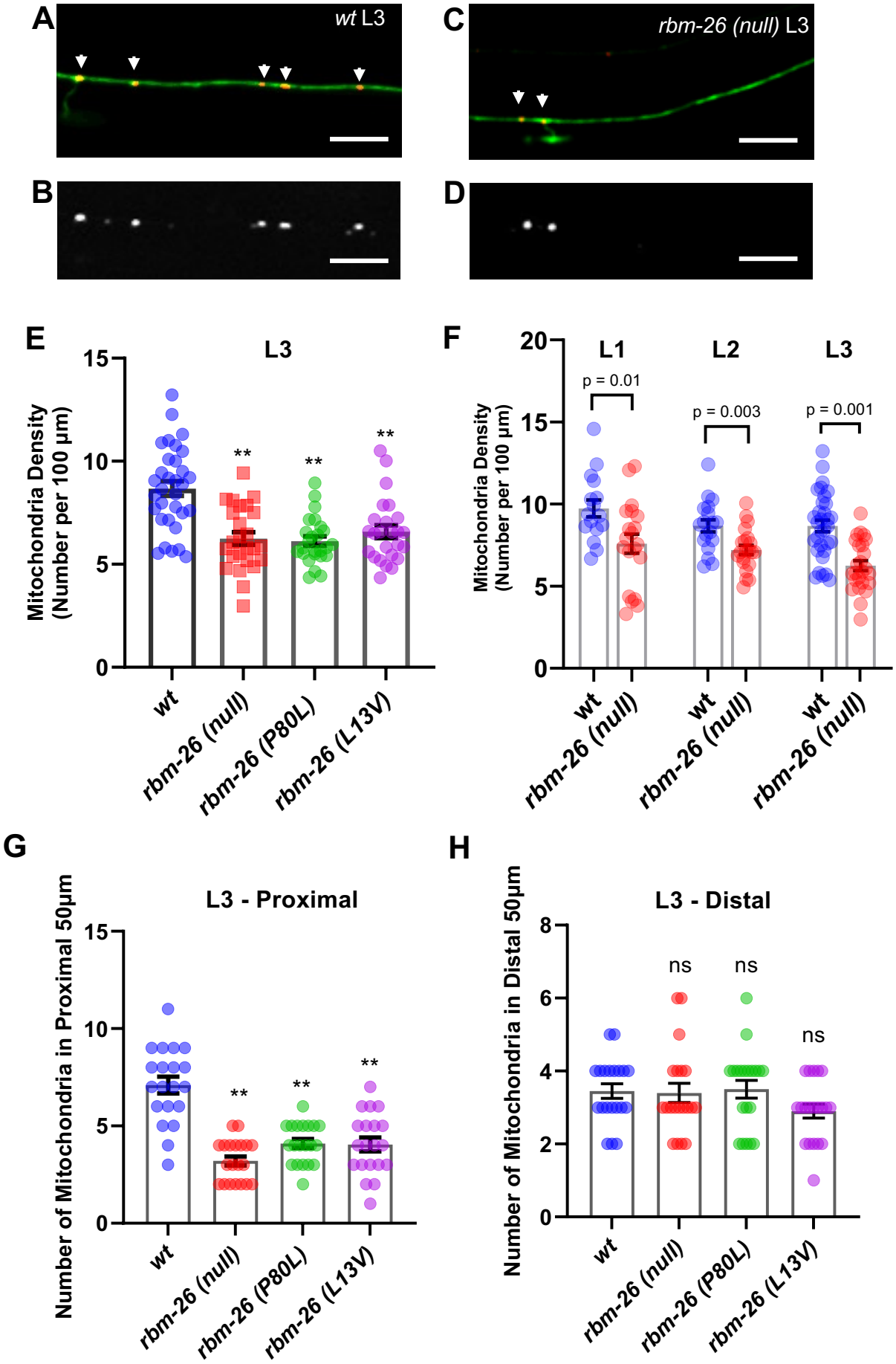
A
wt L3
B
C
rbm-26 (null) L3
D
E
L3
Mitochondria Density (Number per 100 µm)
15
10
5
0
**
**
**
wt
rbm-26 (null)
rbm-26 (P80L)
rbm-26 (L13V)
F
L1
L2
L3
p = 0.01
p = 0.003
p = 0.001
20
15
10
5
0
Mitochondria Density (Number per 100 µm)
wt
rbm-26 (null)
G
L3 - Proximal
Number of Mitochondria in Proximal 50µm
15
10
5
0
**
**
**
wt
rbm-26 (null)
rbm-26 (P80L)
rbm-26 (L13V)
H
L3 - Distal
Number of Mitochondria in Distal 50µm
8
6
4
2
0
ns
ns
ns
wt
rbm-26 (null)
rbm-26 (P80L)
rbm-26 (L13V)

Figure 4

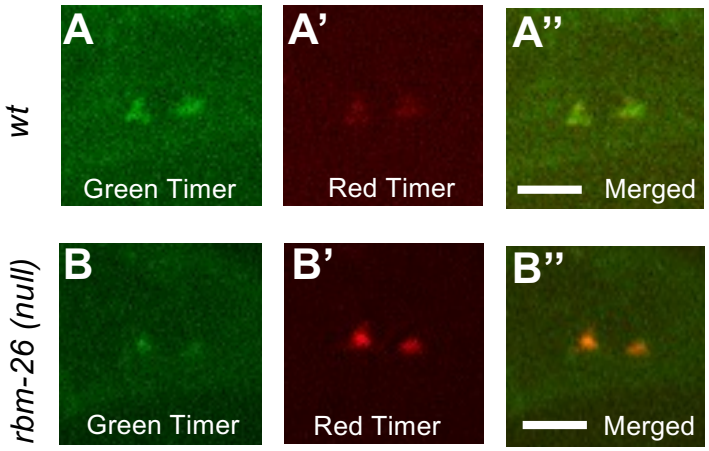
A
A'
A''
wt
Green Timer
Red Timer
Merged
B
B'
B''
rbm-26 (null)
Green Timer
Red Timer
Merged

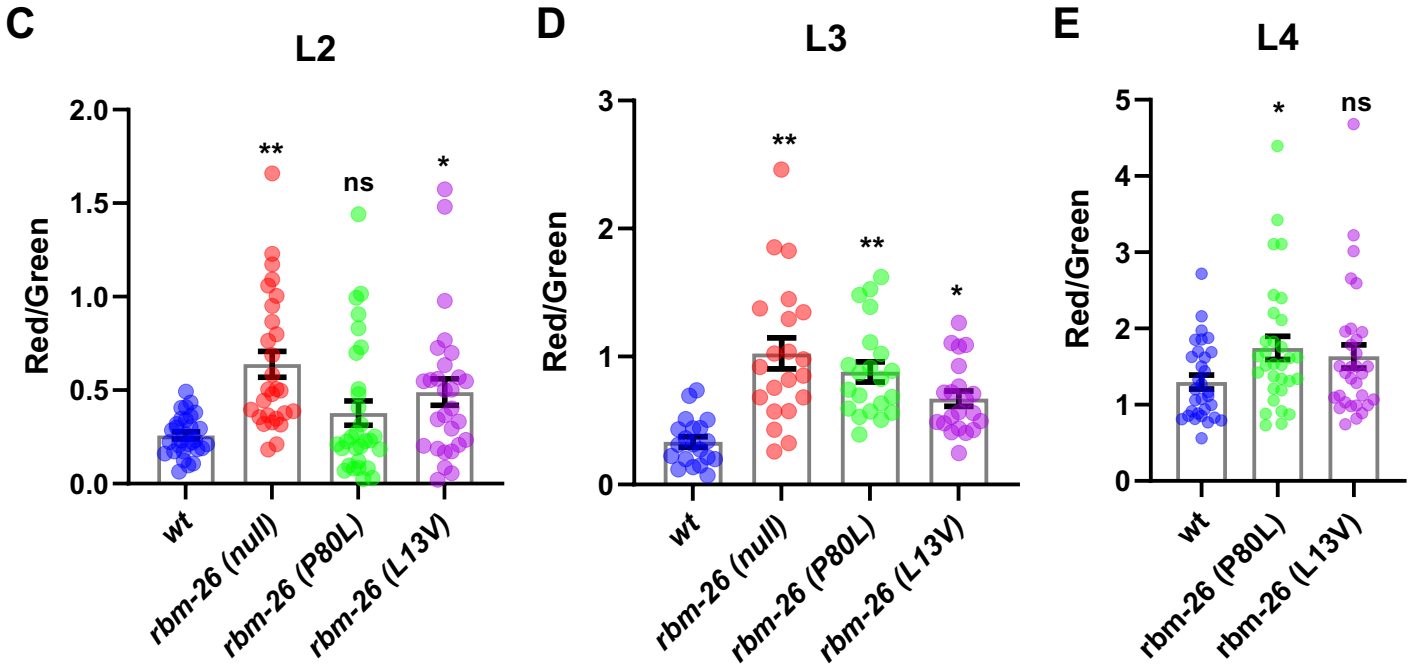
C
L2
Red/Green
2.0
1.5
1.0
0.5
0.0
**
ns
*
wt
rbm-26 (null)
rbm-26 (P80L)
rbm-26 (L13V)
D
L3
Red/Green
3
2
1
0
**
**
*
wt
rbm-26 (null)
rbm-26 (P80L)
rbm-26 (L13V)
E
L4
Red/Green
5
4
3
2
1
0
*
ns
wt
rbm-26 (P80L)
rbm-26 (L13V)

Figure 5

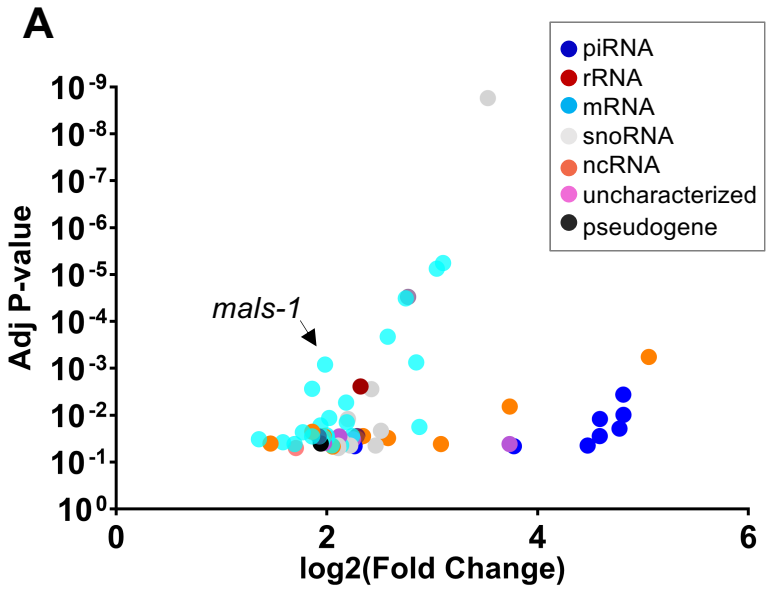
A
piRNA
rRNA
mRNA
snoRNA
ncRNA
uncharacterized
pseudogene
mals-1
Adj P-value
log2(Fold Change)

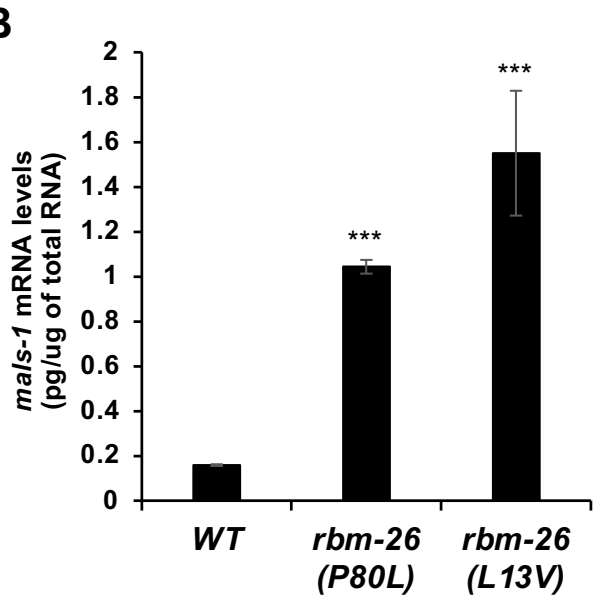
B
mals-1 mRNA levels (pg/ug of total RNA)
***
***
WT
rbm-26 (P80L)
rbm-26 (L13V)

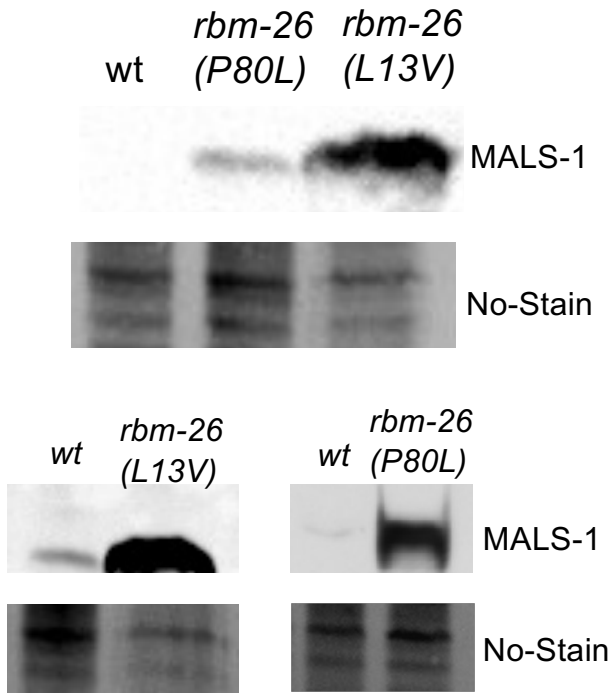
C
wt
rbm-26 (P80L)
rbm-26 (L13V)
MALS-1
No-Stain
wt
rbm-26 (L13V)
wt
rbm-26 (P80L)
MALS-1
No-Stain

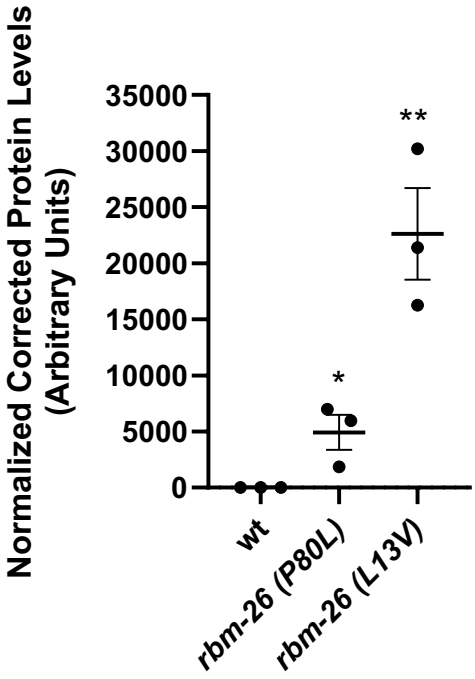
D
Normalized Corrected Protein Levels (Arbitrary Units)
**
*
wt
rbm-26 (P80L)
rbm-26 (L13V)

Figure 6

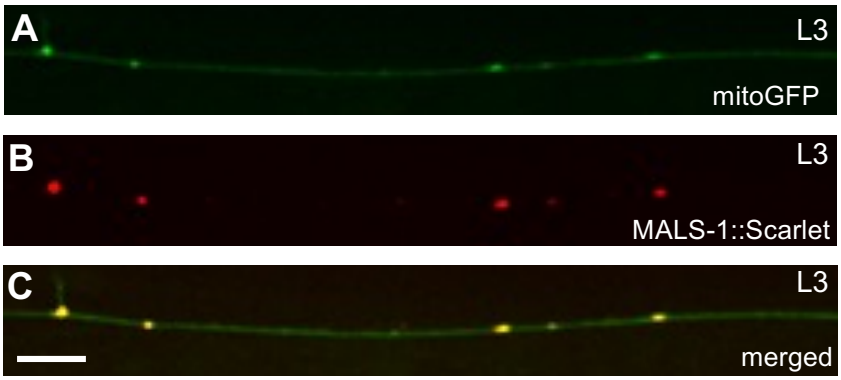
A
L3
mitoGFP
B
L3
MALS-1::Scarlet
C
L3
merged

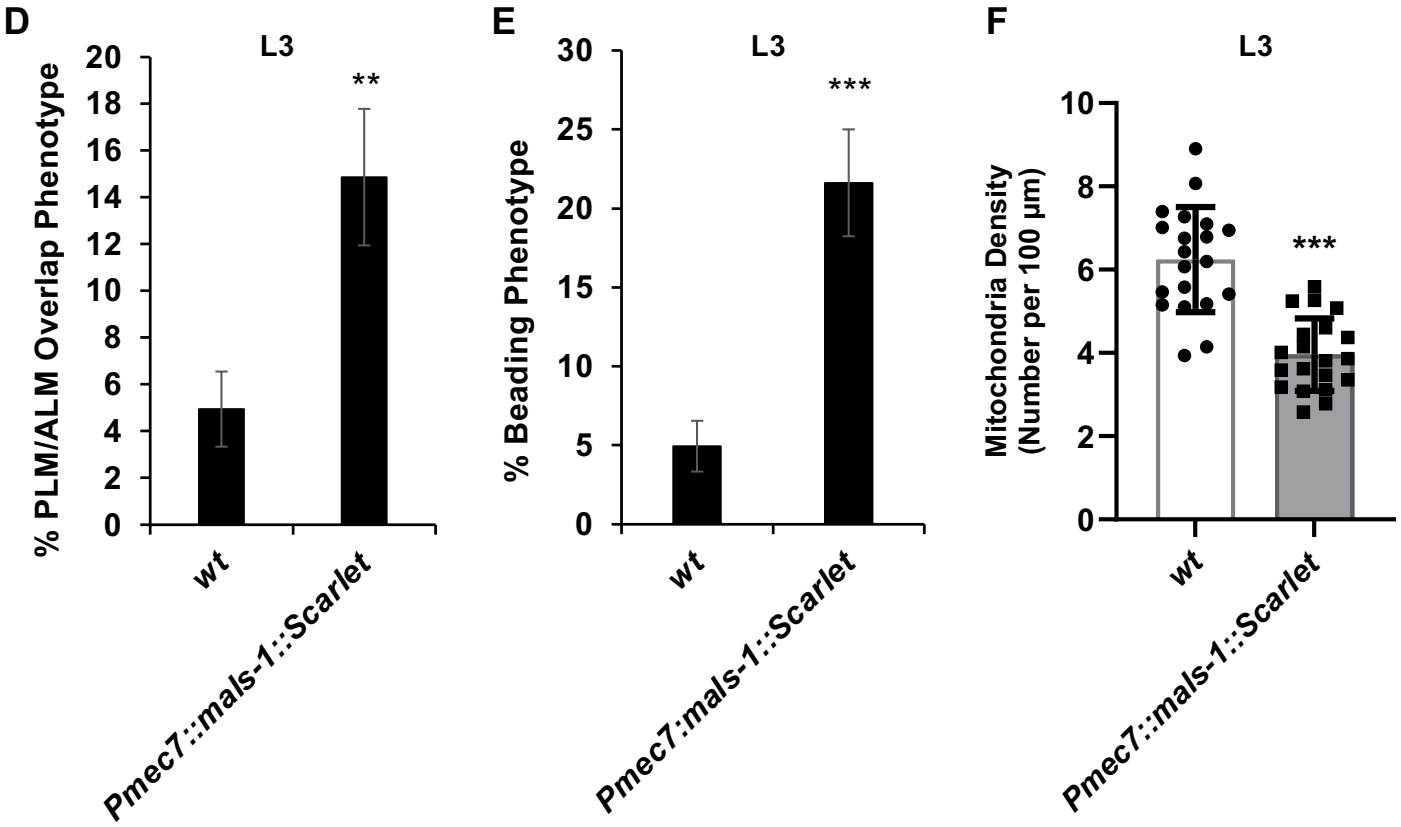
D
L3
% PLM/ALM Overlap Phenotype
20
18
16
14
12
10
8
6
4
2
0
**
wt
Pmec7::mals-1::Scarlet
E
L3
% Beading Phenotype
30
25
20
15
10
5
0
***
wt
Pmec7::mals-1::Scarlet
F
L3
Mitochondria Density
(Number per 100 µm)
10
8
6
4
2
0
***
wt
Pmec7::mals-1::Scarlet

Figure 7

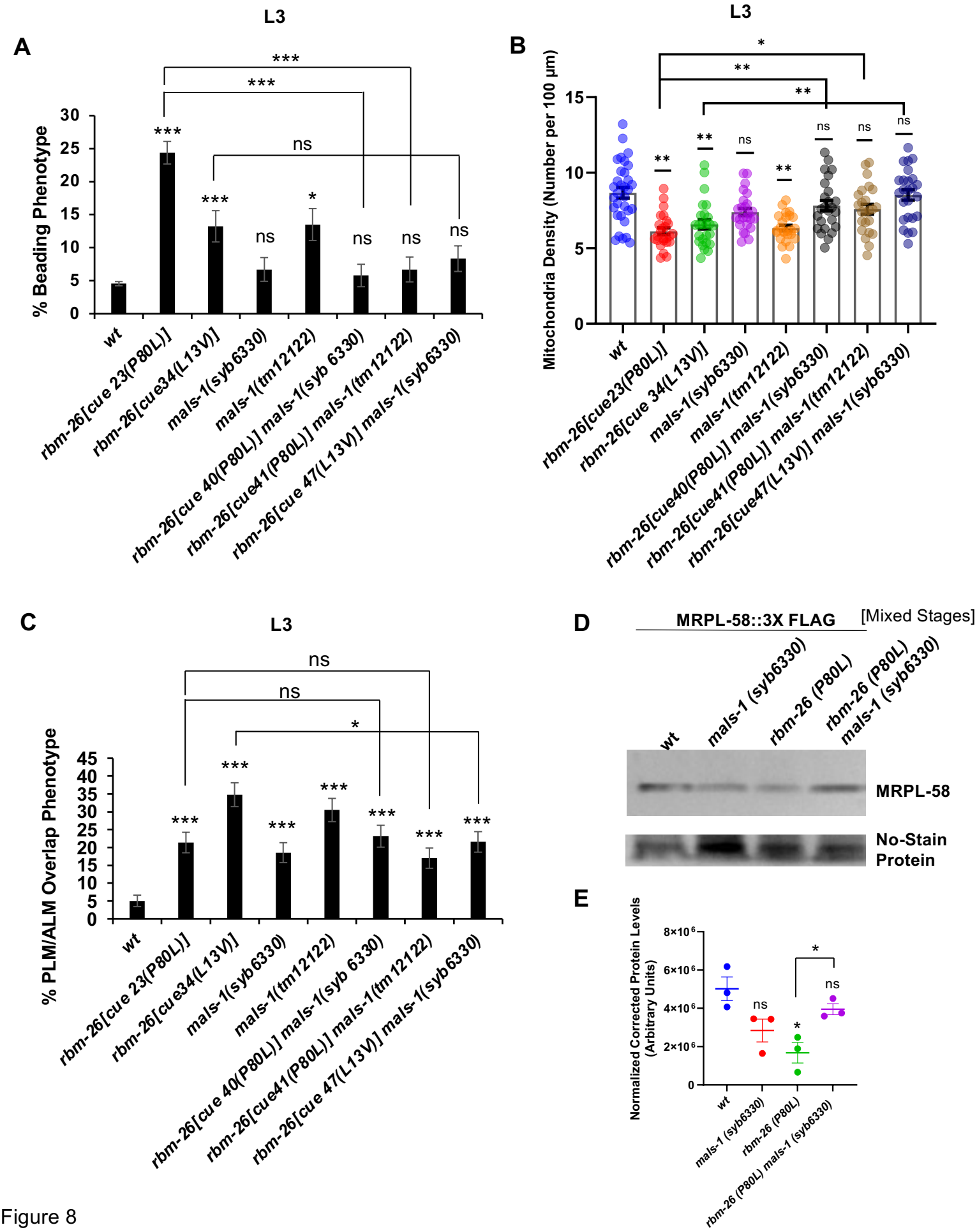
A
L3
% Beading Phenotype
wt
rbm-26[cue 23(P80L)]
rbm-26[cue34(L13V)]
mals-1(syb6330)
mals-1(tm12122)
rbm-26[cue 40(P80L)] mals-1(syb 6330)
rbm-26[cue41(P80L)] mals-1(tm12122)
rbm-26[cue 47(L13V)] mals-1(syb6330)
B
L3
Mitochondria Density (Number per 100 µm)
C
L3
% PLM/ALM Overlap Phenotype
D
MRPL-58::3X FLAG
[Mixed Stages]
wt
mals-1 (syb6330)
rbm-26 (P80L)
rbm-26 (P80L) mals-1 (syb6330)
MRPL-58
No-Stain Protein
E
Normalized Corrected Protein Levels (Arbitrary Units)

Figure 8

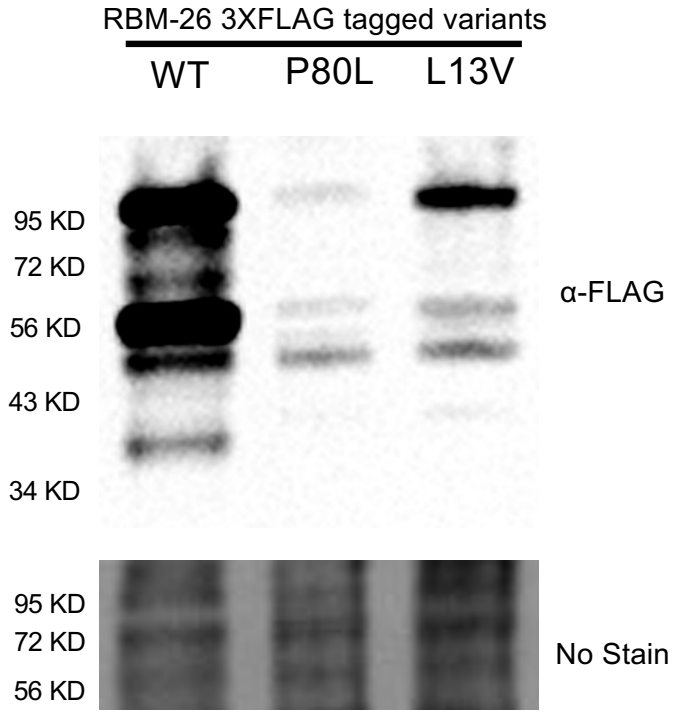

Figure S1: Longer exposure of blot shown in figure 1C. Representative western blot of three biological replicates showing expression of RBM-26::3XFLAG, RBM-26 P80L::3XFLAG and RBM-26 L13V::3XFLAG proteins. 20 µg of total protein lysate was loaded per well and specific proteins were detected with an anti-FLAG antibody and enhanced chemiluminescence. Protein loading was quantified by No-Stain™ Protein Labeling Reagent.

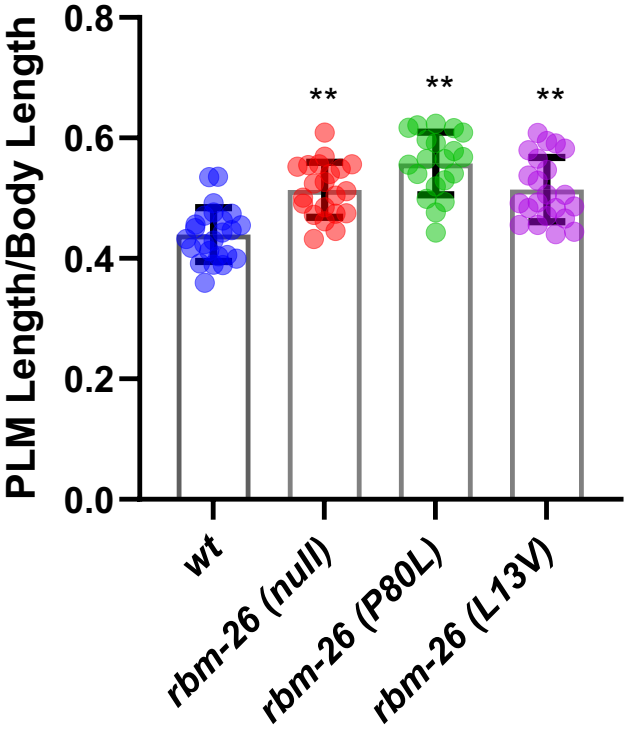

Figure S2: Analysis of PLM axon length suggests that the *rbm-26* mutants cause overextension of the PLM axon. PLM length as a ratio of body length at L3 in wild type (wt), *rbm-26 (null), rbm-26 (P80L) and rbm-26 (L13V)* mutants. Error bars = SD. Statistical significance was analyzed by one-way ANOVA with a Tukey *post hoc* test, ** $p < 0.01$. n for wt = 24, n for *rbm-26 null* = 21, n for *rbm-26 (P80L)* = 20 and n for *rbm-26 (L13V)* = 22. Alleles: *rbm-26(null)* is *rbm-26(gk910)*; *rbm-26(P80L)* is *rbm-26(cue23)*; *rbm-26(L13V)* is *rbm-26(cue34)*

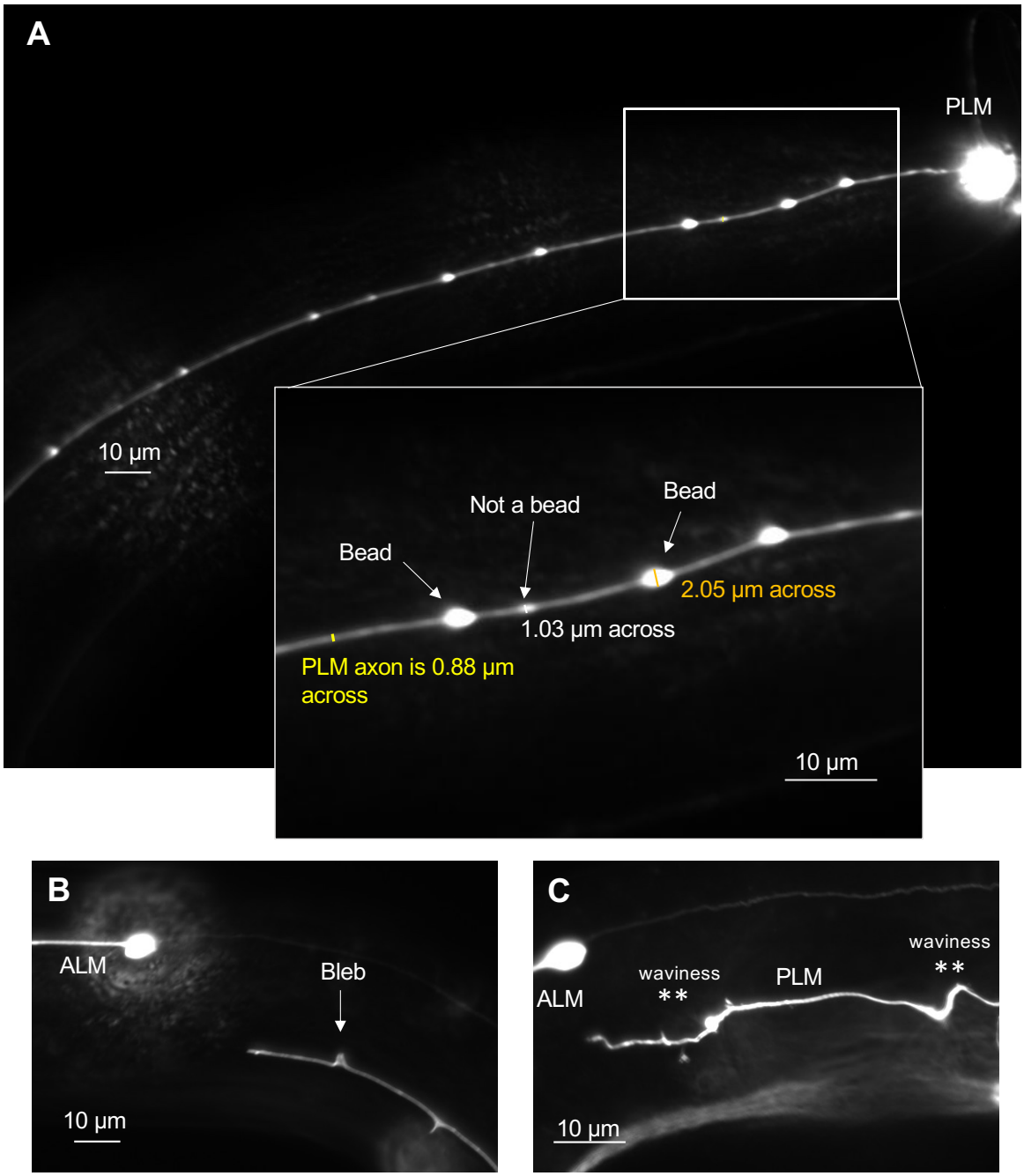

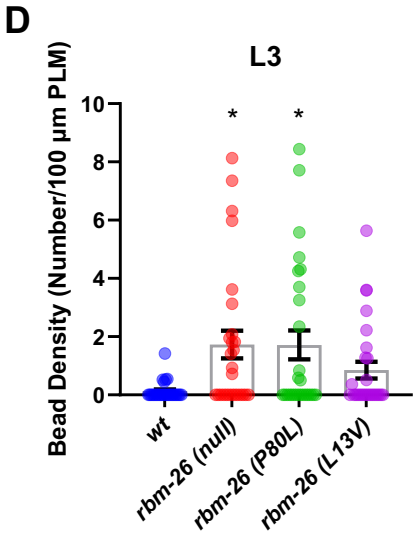

Figure S3: Examples of PLM degeneration phenotypes. (A) Example of beading phenotype. Only those focal enlargements along PLM axon that were at least twice the diameter of the axon were considered to be beads. (B) Example of blebbing phenotype. (C) Example of waviness in PLM axon. (D) Quantification of the bead density (beads per 100 um of PLM axon) observed in wild type (wt), *rbm-26(null)*, *rbm-26(P80L)* and *rbm-26(L13V)* at L3. Error bars are standard error of mean. Statistical significance was analyzed by one-way ANOVA with a Tukey *post hoc* test, * $p < 0.05$ (n = 28).

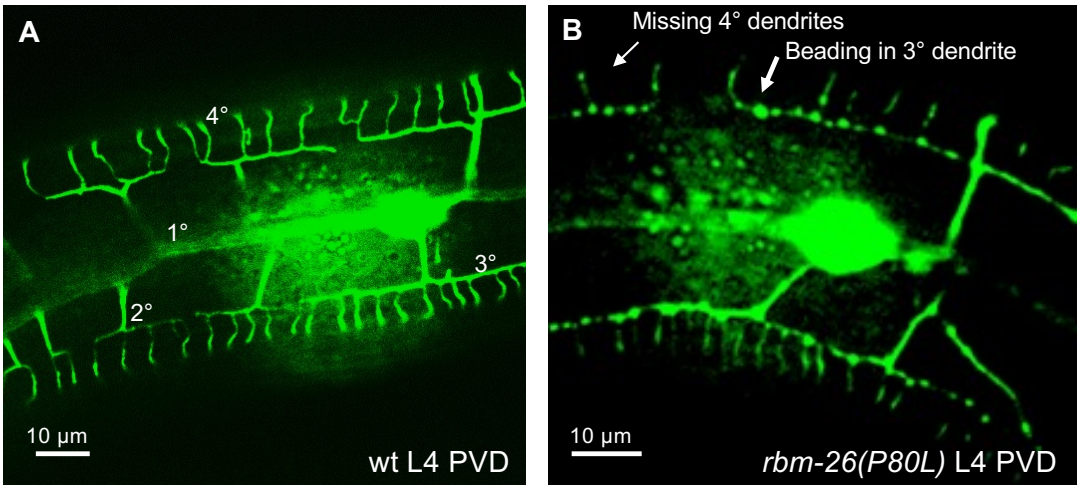

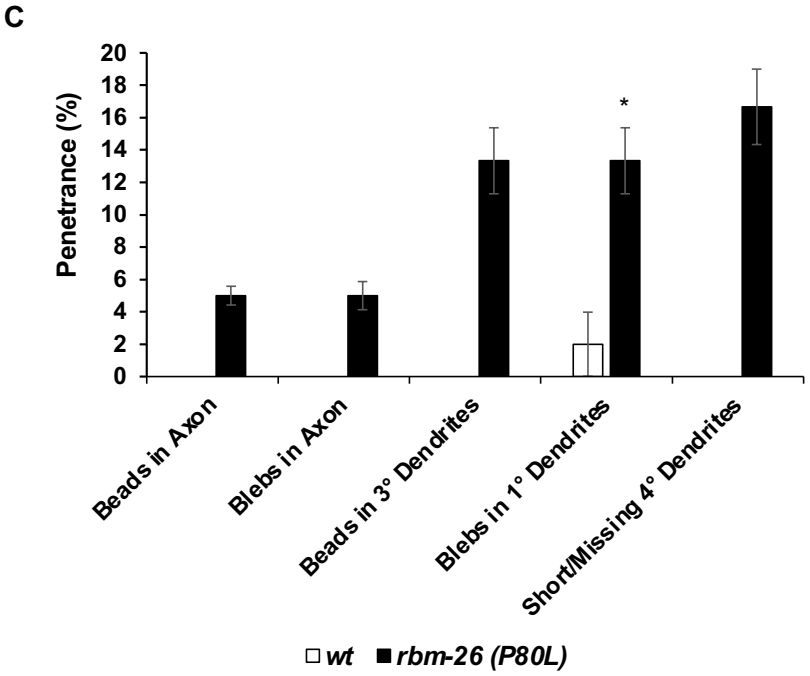

Figure S4. The *rbm-26(P80L)* mutation causes degeneration phenotypes in the axon and dendrites of the PVD neuron. (A) Wild type L4 PVD – primary (1°), secondary (2°), tertiary (3°), and quaternary (4°) dendrites can be seen. (B) Beading can be seen in tertiary dendrites and some quaternary dendrites are missing in *rbm-26(P80L)* L4 PVD neuron. (C) Quantification of phenotypes observed in *rbm-26(P80L)* mutants. 50 wildtype L4 PVD neurons were observed and 60 *rbm-26(P80L)* L4 PVD neurons were observed. PVD neurons were visualized by the *wdIs52 [F49H12.4::GFP + unc-119(+)]* transgene, which expresses GFP in PVD. Asterisks indicate statistically significant difference relative to wild type, Z-test for proportions (* $p<0.05$), and error bars represent the standard error of the proportion.

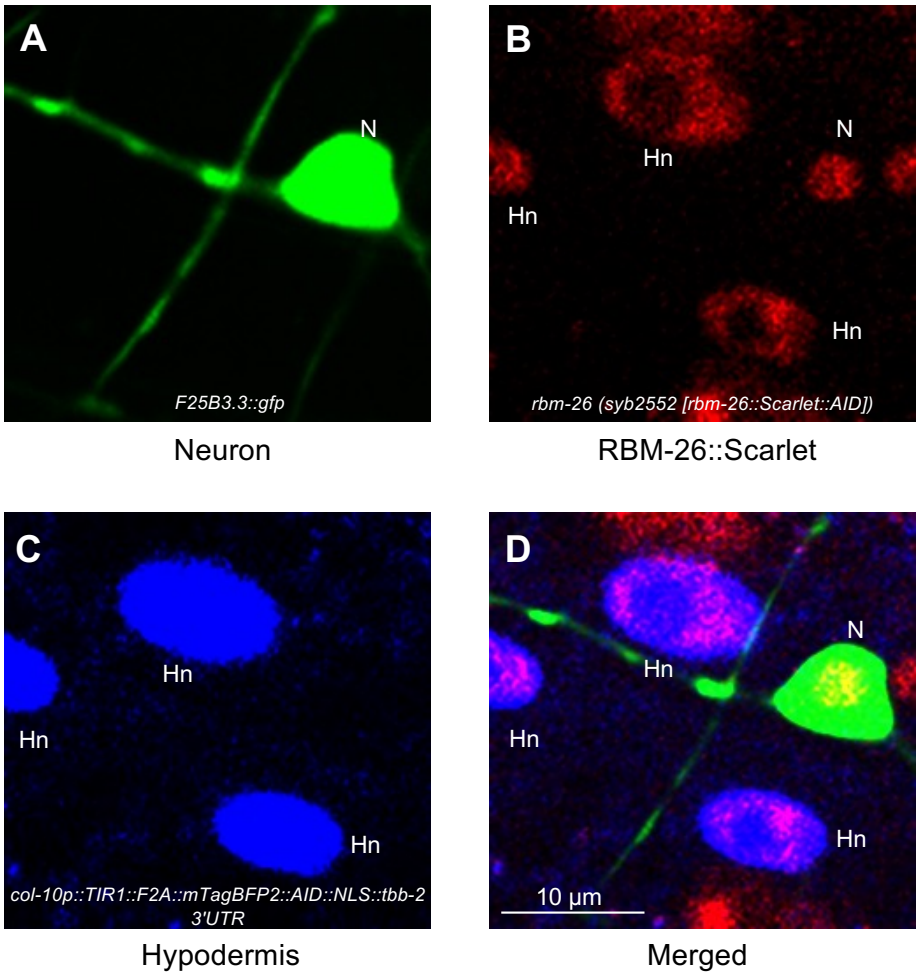

Figure S5. RBM-26 is localized to nuclei in hypodermal and neuronal cells. RBM-26 is expressed in the nuclei of neurons and hypodermal cells. Neurons are identified by the pan-neuronal expression of GFP by the *evIs111* transgene (panels A and D). Hypodermal nuclei are identified by tissue-specific expression of blue fluorescence protein tagged with a nuclear localization signal and an auxin-induced degron *(col-10p::TIR1::F2A::mTagBFP2::AID::NLS::tbb-2 3'UTR)* (panels C and D). Panels B & D show endogenously tagged RBM-26*(rbm-26::Scarlet::AID)*. Panels A – C are merged in D. " N" in panels A, B, and D indicate neuron and "Hn" in panels B, C, and D indicate hypodermal nuclei.

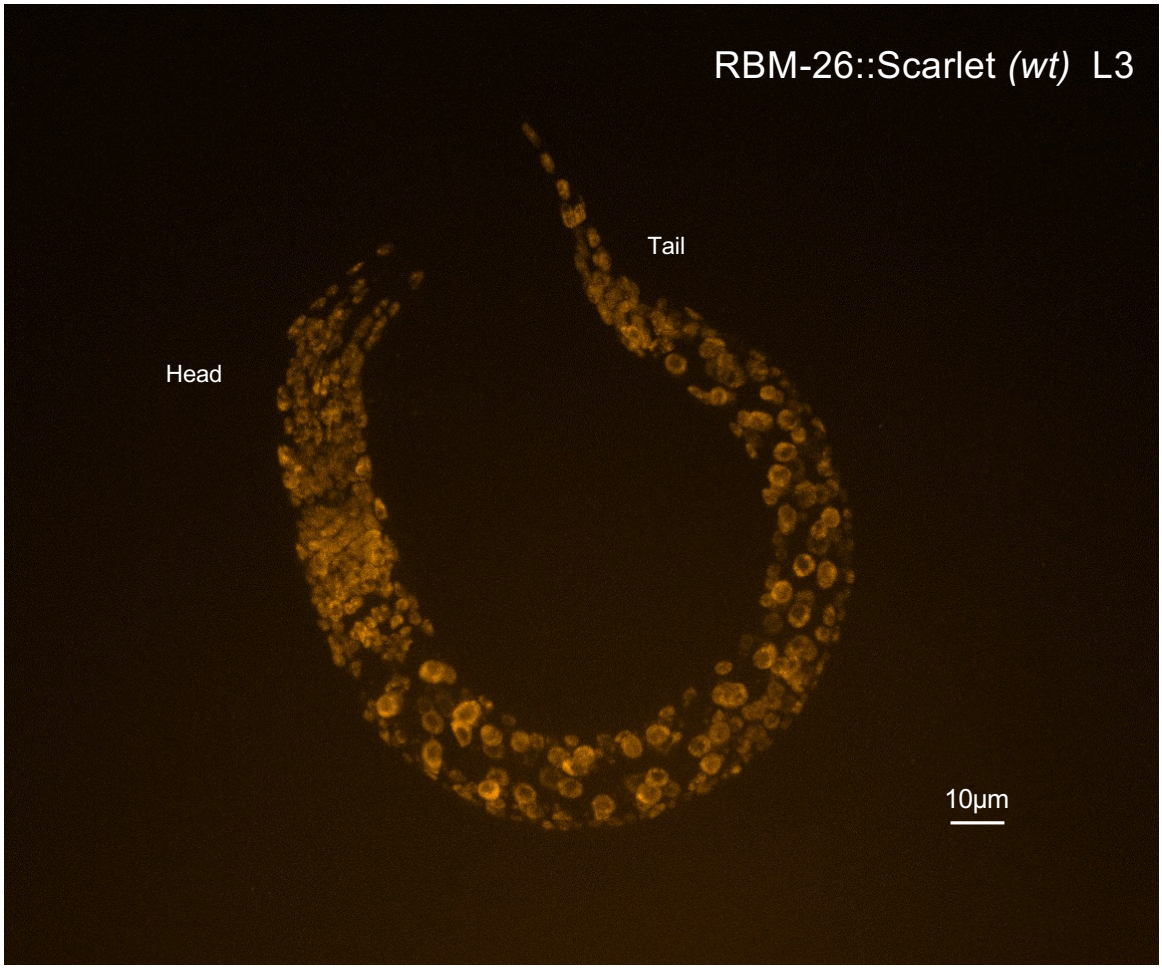

Figure S6: RBM-26 is widely expressed. Representative Z-stack projection of endogenous RBM-26 protein tagged with Scarlet (RBM-26::Scarlet::AID) at larval stage L3.

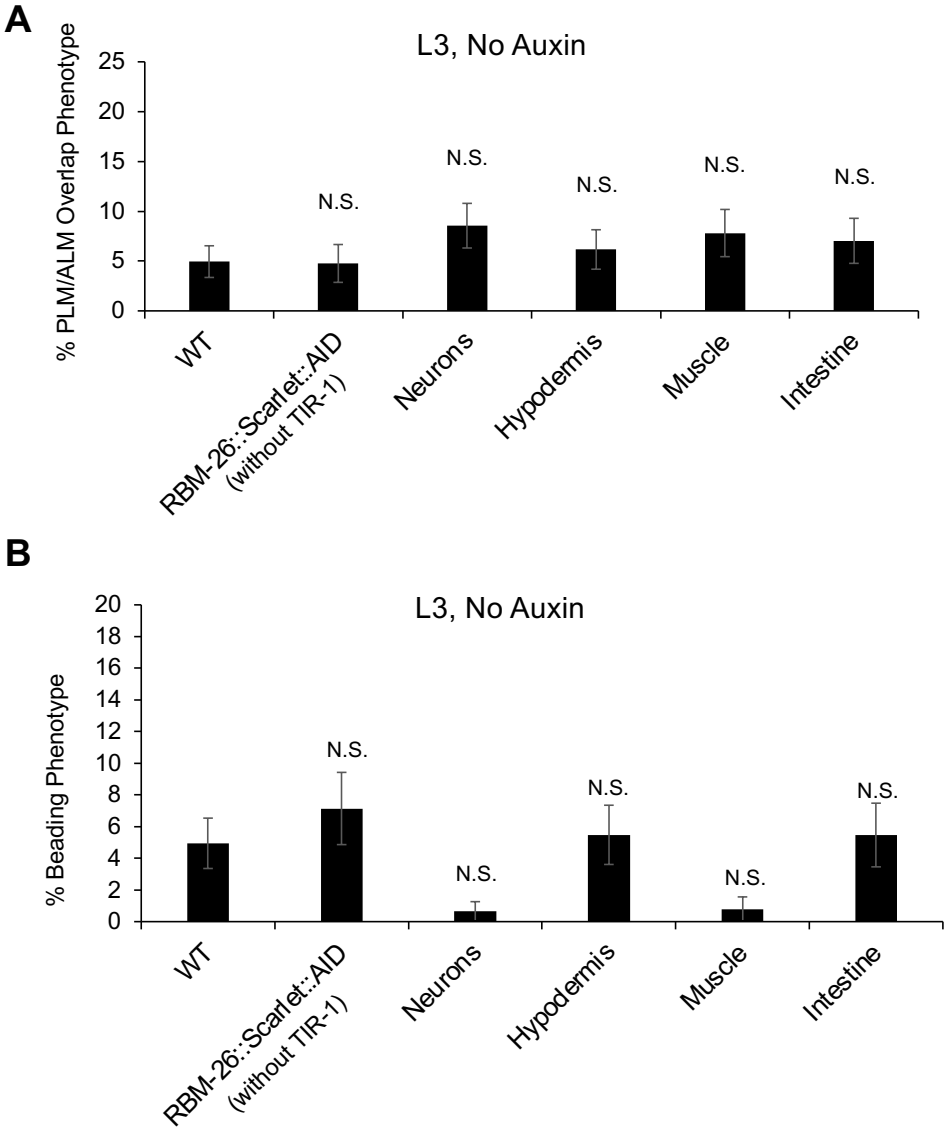

Figure S7: The *rbm-26::Scarlet::AID* gene does not cause the PLM/ALM overlap phenotype (A) or the beading phenotype (B) in the absence of auxin. Worms expressing auxin inducible degron (AID) in frame with RBM-26 and tissue-specific TIR-1 as indicated on the X-axis were placed in Auxin free worm plates at L4 and their progeny were observed at L3. "n" is between 125 and 150. N.S. = not significant (Z-test for proportions). Error bars represent the standard error of the proportion.

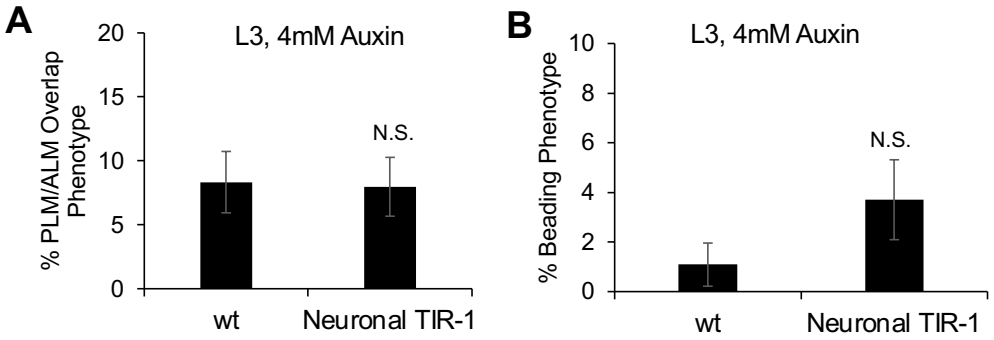

Figure S8: Auxin treatment in the absence of RBM-26::Scarlet::AID does not cause the PLM/ALM axon overlap phenotype or the beading phenotype. L4 wild type or neuronal TIR-1 (without AID tagged RBM-26) were placed on 4 mM synthetic auxin coated plates, allowed to lay eggs and their L3 progenies were analyzed for (A) PLM termination defects and (B) beading phenotypes. "n" is 132 for wt and 138 for Neuronal TIR-1. N.S. = Not Significant (Z-test for proportions). Error bars represent the standard error of the proportion.

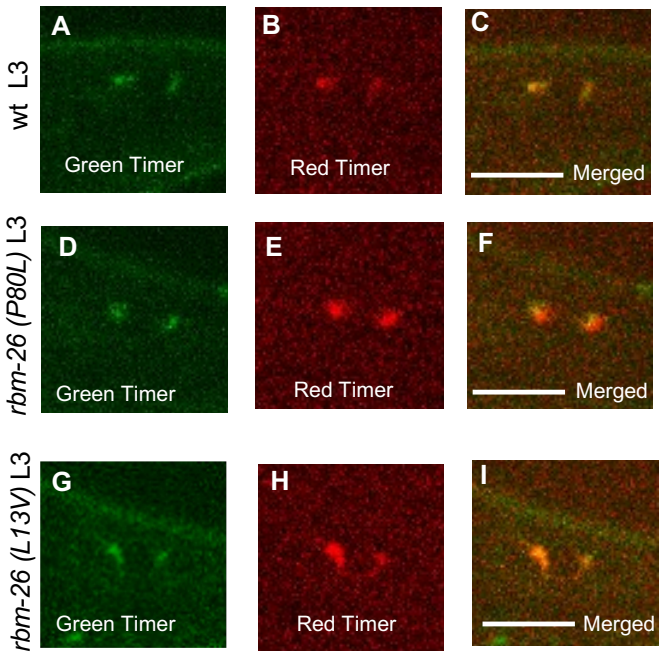

Figure S9. Example of mitoTimer expression in an L3 wild-type [A – C], *rbm-26(P80L)* [D-F] and *rbm-26(L13V)* [E-G] PLM cell bodies. mitoTimer is expressed by the transgene *cueSi35(Pmec-7::mitoTimer::tbb-2 3'UTR)*. Alleles: *rbm-26(P80L)* is *rbm-26(cue23)*; *rbm-26(L13V)* is *rbm-26(cue34).* Scale bars are 5 µm.

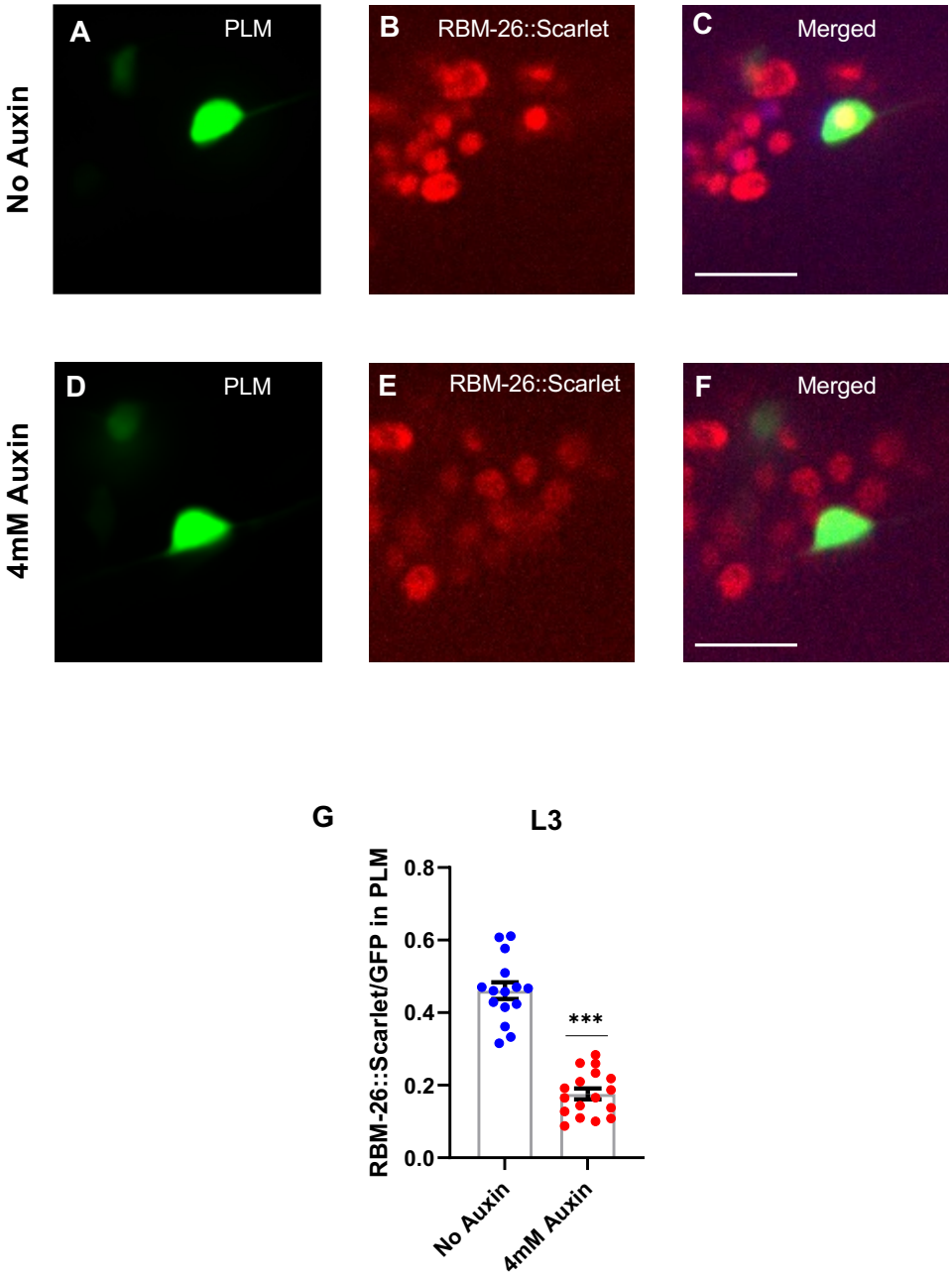

Figure S10: Degron mediated depletion of RBM-26 in PLM. L4 *rbm-26(syb2552); resi7* worms that express RBM-26::Scarlet::AID and F-box Transport Inhibitor Response 1 (TIR-1) in neurons were placed in normal NGM plates (A – C) or on plates coated with 4mM synthetic auxin (D–E), allowed to lay eggs and L3 progeny were analyzed through confocal microscopy. PLM neuron was visualized with the help of the *muIs32 (Pmec-7::gfp)* transgene. Scale bars are 10 µm. Auxin treatment causes depletion of RBM-26 protein, which was quantified in G as a ratio of RBM-26::Scarlet intensity relative to the GFP expression in PLM.

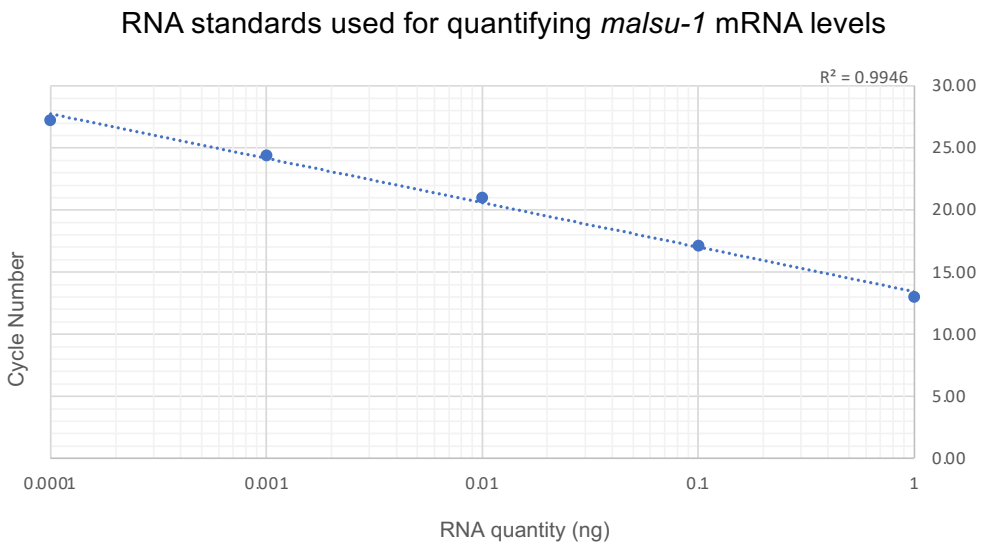

Figure S11: Example of RNA standards used to calculate the quantity of *mals-1* mRNA present in 1 µg of total RNA in wild-type and *rbm-26* mutants *(P80L and L13V)* L4 *C. elegans*. Synthetic RNA corresponding to 68 nucleotides in the last exon and the 3'UTR of *mals-1* mRNA was purchased from Azenta Inc. The RNA was diluted 1 ng/µl, 0.1 ng/µl, 0.01 ng/µl, 0.001 ng/µl, and 0.0001 ng/µl in nuclease free water. The dilutions were quantified in Qubit (Thermo Fisher Scientific) using RNA Qubit Broad Range kit (Thermo Fischer Scientific). 1, 0.1, 0.01, 0.001, 0.0001 ng of RNA standard was used in RT-qPCR reaction. Cycle to threshold (Ct) values obtained from RT-qPCR reaction was plotted against the known quantity of RNA used.

	Age	% Blebbing	% Beading	% Waviness	% Break	N
Wild type	L1	0.925926	1.851852	0	0	108
	L2	0	2.941176	0.980392	0	102
	L3	0	4.545455	1.515152	0	198
	L4	0	6.097561	1.829268	0	164
	1-DAY Adult	0	14.03509	4.385965	0	114
	2-DAY Adult	1.886792	17.92453	0	0.943396	106
rbm-26 (null)	L1	5	0	0	0	80
	L2	2.631579	11.40351	1.754386	0	114
	L3	0	32.36715	13.52657	1.449275	207
	L4	NA	NA	NA	NA	NA
	1-DAY Adult	NA	NA	NA	NA	NA
	2-DAY Adult	NA	NA	NA	NA	NA
rbm-26 (P80L)	L1	1.960784	8.823529	3.921569	0	102
	L2	1.6	15.2	1.6	0	125
	L3	0	24.37811	7.462687	1.492537	201
	L4	2.112676	26.40845	2.112676	2.112676	284
	1-DAY Adult	2.542373	33.89831	4.237288	1.694915	118
	2-DAY Adult	3.448276	62.6506	4.237288	6.024096	118
rbm-26 (L13V)	L1	0.980392	10.78431	2.941176	0	102
	L2	2	8.783784	0.666667	0	150
	L3	1.470588	13.23529	3.333333	0	204
	L4	0.78125	13.88889	2.5	0	128
	1-DAY Adult	0.847458	24.57627	3.389831	0.847458	118
	2-DAY Adult	3.508772	36.84211	3.508772	2.631579	132

Table S1: PLM phenotypes observed in larval stages L1 through L4, one- and two-day adults in wild-type, *rbm-26 (null)*, *rbm-26 (P80L)* and *rbm-26 (L13V)* worms. Maternally rescued *rbm-26 (null)* worms do not survive past L3.

Gene.name	Human Ortholog (HGNC Symbol)	log2FoldChange	padj
F59C6.15	NA	3.529339	1.70E-09
pud-2.1	NA	3.103615	5.63E-06
pud-2.2	NA	3.04405	7.45E-06
pud-1.1	NA	2.772255	2.98E-05
pud-1.2	NA	2.749208	3.21E-05
C23H5.8	NA	2.578636	0.00021
C37A2.9	NA	5.056751	0.000568
ilys-5	NA	2.848721	0.000745
K12H4.2 (mals-1)	MALSU1	1.983865	0.000826
rrn-2.1	NA	2.319809	0.002424
clec-85	NA	1.860425	0.00272
K07C5.11	NA	2.422354	0.002764
21ur-8178	NA	4.814433	0.003612
spp-4	NA	2.183194	0.005335
Y6B3B.13	NA	3.736574	0.00653
21ur-3462	NA	4.815693	0.009799
K02A11.4	NA	2.023582	0.011462
21ur-10303	NA	4.592398	0.01198
F43A11.8	NA	2.201064	0.01198
F33H12.7	NA	2.189781	0.014145
msp-81	NA	1.939555	0.01655
fip-7	NA	2.878975	0.017713
21ur-12103	NA	4.77819	0.019219
Y46G5A.40	NA	2.514422	0.021423
F55A8.4	NA	1.86247	0.022547
clc-1	NA	1.772934	0.023129
clec-209	NA	1.99952	0.026991
21ur-7931	NA	4.59147	0.027738
F59D8.3	NA	2.344256	0.027738
F22D6.16	NA	2.290677	0.027738
K07C5.18	NA	2.283691	0.027738
K06A4.7	NA	2.239518	0.027738
T19C4.17	NA	1.972172	0.027738
D1065.7	NA	2.118396	0.028351
C33H5.13	NA	1.929031	0.028351
dpy-4	MARCO	1.922891	0.028351
Y75B8A.28	NA	1.860966	0.028351
F28H7.3	NA	1.968765	0.029705
Y38H6C.23	NA	2.002049	0.029819
Y40B1A.5	NA	2.581652	0.030633
T27A10.8	NA	2.290521	0.031615
C08F11.116	NA	2.249682	0.032408
F16H6.10	NA	1.354888	0.032408
F56A4.2	NA	1.954246	0.035992
Y43F8C.22	NA	2.149066	0.03674
gst-22	GSTA1/GSTA2/GSTA3/GSTA4/GSTA5	1.583856	0.037515
W05H9.3	NA	1.974427	0.039296
F07H5.3	NA	1.942375	0.040116
F54B11.14	NA	1.465389	0.040116
C05E7.t2	NA	3.735348	0.041196
W02F12.11	NA	3.084148	0.041196
T19C9.8	NA	1.693645	0.041196
acdh-1	ACADS/ACADSB	2.136673	0.043721
lys-4	NA	2.048744	0.043721
21ur-7165	NA	4.475939	0.04407
F18C5.15	NA	2.463115	0.04407
H04D03.5	NA	2.223033	0.04407
JC8.15	NA	2.10709	0.04407
21ur-5454	NA	3.776464	0.045548
21ur-10438	NA	2.263752	0.045548
C18E9.14	NA	2.055965	0.046461
ZK546.18	NA	2.109542	0.049805
rme-2	LRP3/LRP12/LDLRAD3/LRP10	1.706674	0.049881

Table S2: RNA interactors of RBM-26 identified by RNA immunoprecipitation followed by RNASeq. Human orthologs were identified with Orhtolist2 (Woojin Kim, Ryan S Underwood, Iva Greenwald, Daniel D Shaye, OrthoList 2: A New Comparative Genomic Analysis of Human and *Caenorhabditis elegans* Genes, *Genetics*, Volume 210, Issue 2, 1 October 2018, Pages 445–461). NA = Human Ortholog not found.

Genotype	Source
rbm-26(cue23[rbm-26 (P80L)]) III	This Study
rbm-26(cue34[rbm-26 (L13V)]) III	This Study
rbm-26(cue25[rbm-26::3X FLAG]) III	This Study
rbm-26(cue22[rbm-26 (P80L)] cue25[rbm-26::3X FLAG]) III	This Study
rbm-26(cue24[rbm-26 (L13V)] cue25[rbm-26::3X FLAG]) III	This Study
mals-1(cue37[mals-1::3X FLAG]) III	This Study
mals-1(syb6330) III	SUNY Biotech
rbm-26(cue40[rbm-26(P80L)]) mals-1(syb6330) III	This Study
rbm-26(cue42[rbm-26(P80L)]) mals-1(cue37 [mals-1::3X FLAG]) III	This Study
mals-1(tm12122) III	Mitani Lab, International C. elegans Gene Knockout Consortium
rbm-26(cue 41[rbm-26(P80L)]) mals-1(tm12122) III	This Study
mrpl-58(cue38[mrpl-58::3XFLAG]) III	This Study
rbm-26(cue39[rbm-26 (P80L)]) mrpl-58(cue 38 [mrpl-58::3X FLAG]) III	This Study
rbm-26(cue 47[rbm-26 (L13V)]) mals-1(syb6330)] III	This Study
rbm-26(syb2552[rbm-26::Scarlet::AID]) III	SUNY Biotech
rbm-26(cue 48[rbm-26 (P80L)]) syb2552[rbm-26::Scarlet::AID]) III	This Study
cueSi35(Pmec-7::mitoTimer::tbb-2 3'UTR) IV	this study
cueSi36(Pmec-7::mals-1::scarlet::tbb-2 3'UTR) IV	this study
evIs111[F25B3.3::GFP + dpy-20(+)]; rbm-26(syb2552[rbm-26::Scarlet::AID]) III; reSi1[col-10p::TIR1::F2A::mTagBFP2::AID::NLS::tbb-2 3'UTR] I*	this study
muIs32[mec-7p::GFP + lin-15(+)]	CGC
muIs32[mec-7p::GFP + lin-15 (+)]; rbm-26(cue23[rbm-26 (P80L)]) III	this study
muIs32[mec-7p::GFP + lin-15 (+)]; rbm-26(gk910) III/hT2 [bli-4(e937) let-?(q782) qIs48] I;III	this study
muIs32[mec-7p::GFP + lin-15 (+)]; rbm-26(cue34 [rbm-26 (L13V)]) III	this study
muIs32[mec-7p::GFP + lin-15(+)]; rbm-26(syb2552 [rbm-26::Scarlet::AID]) III	this study
muIs32[mec-7p::GFP + lin-15(+)]; rbm-26(syb2552 [rbm-26::Scarlet::AID]) III; reSi1[col-10p::TIR1::F2A::mTagBFP2::AID::NLS::tbb-2 3'UTR] I*	this study
muIs32[mec-7p::GFP + lin-15(+)]; rbm-26(syb2552 [rbm-26::Scarlet::AID]) III; reSi7[rgef-1p::TIR1::F2A::mTagBFP2::AID::NLS::tbb-2 3'UTR] I*	this study
muIs32[mec-7p::GFP + lin-15(+)]; rbm-26(syb2552 [rbm-26::Scarlet::AID]) III; reSi3[unc-54p::TIR1::F2A::mTagBFP2::AID::NLS::tbb-2 3'UTR] I*	this study
muIs32[mec-7p::GFP + lin-15(+)]; rbm-26(syb2552 [rbm-26::Scarlet::AID]) III; reSi12[ges-1p::TIR1::F2A::mTagBFP2::AID::NLS::tbb-2 3'UTR] II*	this study
jsIs1073[mec-7p::TagRFP-mito::CBunc119]	Obtained from Michael Nonet
jsIs1073[mec-7p::TagRFP-mito ,CBunc119]; rbm-26(gk910) III/hT2[bli-4(e937) let-?(q782) qIs48] I;III	this study
jsIs609[mec7p::mtGFP + lin-15(+)] X	Obtained from Michael Nonet
jsIs609[mec7p::mtGFP + lin-15(+)] X; cueSi36(Pmec-7::mals-1::scarlet::tbb-2 3'UTR) IV	this study
cueSi35(Pmec-7::mitoTimer::tbb-2 3'UTR) IV; rbm-26(gk910) (III)/hT2 [bli-4(e937) let-?(q782) qIs48] (I;III)	this study
cueSi35(Pmec-7::mitoTimer::tbb-2 3'UTR) IV; rbm-26(cue23 [rbm-26(P80L)]) III	this study
*wbmIs67[eft-3p::3XFLAG::wrmScarlet::unc-54 3'UTR *wbmIs65] V*	CGC
*wbmIs72[pie-1p::3XFLAG::GFP::unc-54 3'UTR *wbmIs60] III*	CGC
cueSi52(Pmec-7::rbm-26::scarlet::unc-54 3'UTR) IV	this study
rbm-26(cue49[rbm-26(L13V)] mals-1(cue37[mals-1::3XFLAG]) III	this study
mrpl-58(cue50 [mrpl-58::3XFLAG]) mals-1(syb6330) III	this study
rbm-26(cue51[rbm-26(P80L)] mrpl-58(cue50 [mrpl-58::3XFLAG]) mals-1(syb6330) III	this study

Table S3: Strains used in this study

Table S4: Resource Tables

Primers used in figure 5B
TGCACGAAGGAGCACAAAAC (forward)
CGTGCACCTGAACTCTTTCC (reverse)

Antibodies used in this study

Antibody	Catalog Number	Manufacturer	Dilution
DYKDDDDK Tag Antibody	2368S	Cell Signaling Technology	1:1000
Goat Anti-Rabbit IgG H&L (HRP)	ab205718	Abcam	1: 5000

CRISPR reagents used in this study

CRISPR edit	guide RNA	Homology Directed Repair Template
rbm-26 (P80L)	CACAAGCAAAAGCTATATGC	GCAGTTGCTGAAGCAGAGGTAGGCGCTGTTGATGCAAGCATATAGCTTTTGCTAGTGAGTGCTTCGAAGACTTTGTCGACGAATGGAGCAGT
rbm-26 (L13V)	ATGAGGATGCTCTCTTCGAT	GGCTGTCTAATCAATGAAAAAACTTACATTGGCGAGAGCTCATCAGAGACCCAGTCGAAAAGAGCATCCTCATTGTCGATGTGCATGCTTTCTTTGATATT
rbm-26 (3X FLAG)	ACTAGGACTAATCATTTAGC	ATTTTGAGATCAAAGTTCTAATATAACTAGGACTATTTATCGTCATCGTCTTTGTAGTCGATATCGTGATCTTTGTAGTCGCCATCGTGATCTTTGTAGTCATCATTTAGCAGGTCATCTTCTTCGTCAGACTGAAATCTATCATTTAGCAGGTCATCTTCTTCGTCAGACTGAAATCT
mals-1 (3X FLAG)	AAAGGAAAACATTATCGTCT	CAATAATCTAAATGTTATAAATAACAAAAGGAAAACATTACTTGTCATCGTCGTCTTTGTAGTCGATGTCGTGATCCTTATAATCGCCGTCGTGGTCCTTGTAGTCTCGTCTCGGTGGCAGCAAAATCTTCTGTTTCTCCTCATCAATCTCG
mrpl-58 (3X FLAG)	GCTAATTAGCTAAAACTCAA	GGAAAAATAAAACACGAACAAAATTTCAGCTAATTAGCTACTTGTCATCGTCGTCTTTGTAGTCGATGTCGTGATCCTTATAATCGCCGTCGTGGTCCTTGTAGTCAAACTCAACGGCGGCTCGTCGCGACGCCTTTTTCTCACTCGTTCT